Chapter 4

Stagnation flow and flame simulations

Knowledge itself is power.—Francis Bacon

4.1 The laminar impinging jet—Cold flow

4.1.1 Introduction

Axisymmetric jets impinging perpendicularly on a wall are encountered in a variety of real-life situations such as Chemical Vapor Deposition (CVD) processes (Goodwin, 2003). Although the fluid mechanics of the wall-impinging jets are interesting phenomena in their own right, this topic is studied here for two reasons. The first is to assess the extent to which experimental data and numerical data agree when no chemical reactions are involved. In particular, since this is the case in which the modeling error is expected to be small as the incompressible Navier-Stokes equations are known to describe uniform density flow well, any uncertainty between measurements and computation will be quantified. The second objective is to learn the general behavior of stagnation flow to apply the knowledge of non-reacting flow to reacting cases. In this study, the nozzle-to-plate separation distance L to nozzle-diameter d ratio range of $0.5 \leq L/d \leq 1.5$ is studied. This range of L/d has been investigated experimentally and is useful in the study of strain-stabilized flames in combustion research.

This type of flow has a well-known approximate similarity solution presented in Schlichting (1960), called Hiemenz flow. This similarity solution is based on an analytical solution for potential flow and used to develop the one-dimensional stagnation flame or opposed-jet

flame model by Kee *et al.* (1988). This was a very useful extension in combustion research and many studies use this one-dimensional formulation, although it has rarely been used to study non-reacting flow, as more-detailed multidimensional simulations are available for such cases. However, there are not many numerical studies reported for the separation distances that enable us to draw a conclusion about whether a one-dimensional model is a good approximation for stagnation flows with small separation distances. For example, Deshpande & Vaishnav (1982) studied an axisymmetric round jet impinging on a wall for $L/d = 1.5$ and 2. Pelletier *et al.* (2004) also studied axisymmetric laminar and turbulent impinging round jets using the finite element method, at separation distances of $L/d = 1$, 2, and 4. Nothing shorter than these separation distances has been reported to the author's knowledge.

In the present study, a simulation of cold flow laboratory experiments reported by Bergthorson *et al.* (2005a) is conducted by including parts of the nozzle-plenum assembly in the computational domain as well as the stagnation plate. A smaller flow enclosure is used compared to the original experiments to save computational time without sacrificing accuracy. In addition, the behavior of the one-dimensional model developed by Kee *et al.* (1988) is assessed.

For the axisymmetric two-dimensional simulation of a laminar impinging jet with a separation distance $L/d = 1.424$, the computational domain shown in Fig. 4.1 is used, which appropriately models the corresponding experiments conducted by Bergthorson *et al.* (2005a).

A study of the effects of boundary conditions on the flow field was undertaken to ascertain that the flow field near the stagnation point was insensitive to the particular choice of the boundary conditions away from the region of interest. A nearly flat velocity profile is introduced at the nozzle inlet, just downstream of the last turbulence-management grid and before the beginning of the nozzle contraction (Fig. 4.1): $u_1(r)/U_\mathrm{P} = \tanh[c_1(1 - r/r_\mathrm{P})]$, where $r_\mathrm{P} = d_\mathrm{P}/2$ is the radius of the plenum, U_P is the centerline velocity at the plenum, and c_1 is set to 50. This profile mimics the outflow from the turbulence-management section in the experiments. As expected, the jet profile at the nozzle exit is insensitive to the choice of inlet profile, owing to the high contraction ratio in the nozzle design. Shown in Fig. 4.2 is a simulated axial-velocity profile at the nozzle exit compared with a Pitot-probe measurement along a line that cut through the axis. Both simulation and experiments are conducted

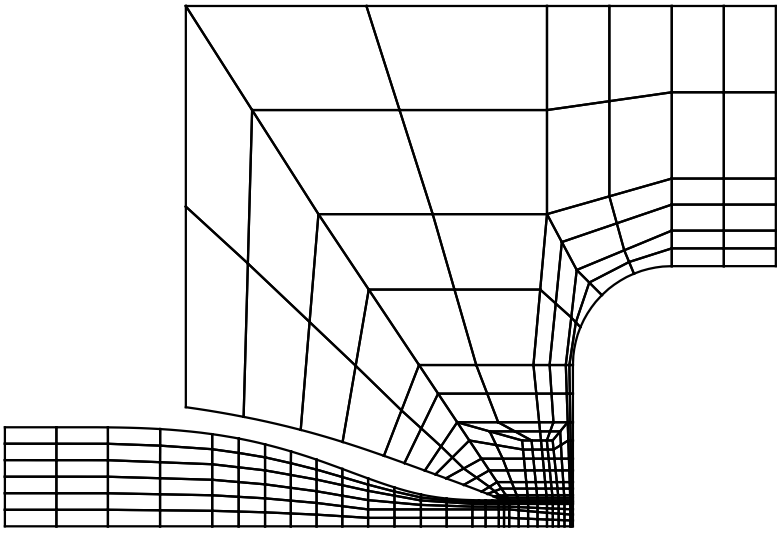

Figure 4.1: A computational domain used for the simulation of non-reacting stagnation flow. It incorporates 360 elements, within which 6 by 6 mesh collocation points are used.

without the stagnation plate to observe the characteristics of the nozzle. The well-designed contraction nozzle produces a flat velocity profile, and the simulation, which incorporates the shape of the nozzle interior as specified in Bergthorson *et al.* (2005a), captures the velocity profile accurately. The slight disagreement between simulation and experiment in the wall boundary layer region is attributable to the finite pitot-probe extent, d_{pitot}, in the radial direction, for which no corrections were applied (Bergthorson *et al.*, 2005a).

To simulate the entrained flow, an entrainment flux is introduced through the lower portion of the outer domain (top left). It was shown that the particular choice of entrainment flux does not affect the velocity field in the near-field region of interest ($0 \leq r/d \leq 1$, $-L/d \leq z/d \leq 0$), more than a percent (Bergthorson *et al.*, 2005a). A uniform-pressure condition is specified at the outflow between the flow enclosure and the stagnation plate (top right).

Results presented in this section were presented in Bergthorson *et al.* (2005a).

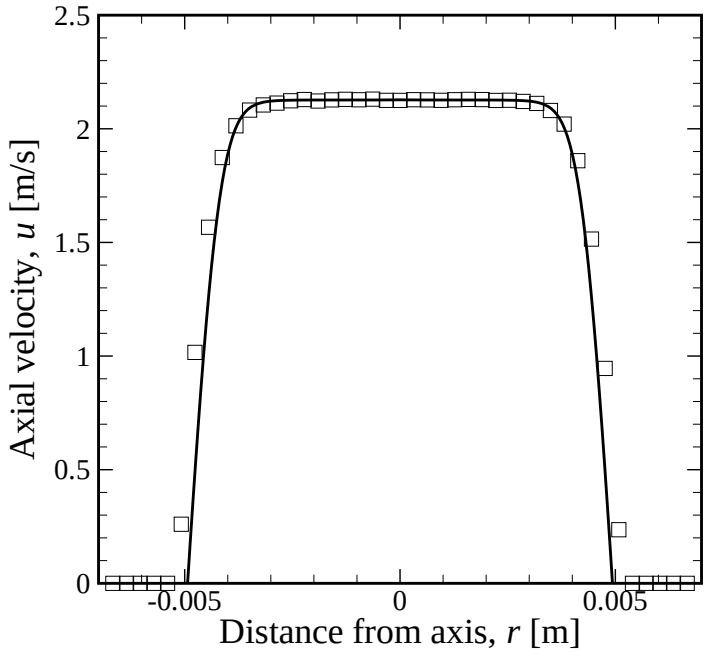

Figure 4.2: Axial velocity profile at the nozzle exit. The internal diameter of the nozzle at the opening is 9.9×10^{-3} m and the Reynolds number of the jet based on the centerline axial velocity is about 1400. (Solid line) simulation; (□) measurements

4.1.2 Results and discussion

4.1.2.1 Comparison to experiments

Experimental velocity data reported in Bergthorson *et al.* (2005a) were recorded at three nominal Reynolds numbers,

$$Re \equiv \frac{\rho\, d\, u_{\mathrm{B}}}{\mu} \cong 400\,,\ 700\,,\ \text{and } 1400, \tag{4.1}$$

with actual values within ±35 in each case, and at three nozzle-to-stagnation-plate separation distance to nozzle-exit-diameter ratios, $L/d \cong 0.7$, 1.0, and 1.4. The reference velocity, u_{B}, is called the Bernoulli velocity and is defined by

$$u_{\mathrm{B}} = \sqrt{\frac{2\Delta p/\rho}{1-(d/d_p)^4}}. \tag{4.2}$$

One could use the centerline axial velocity at the nozzle exit, u_0, as the reference velocity. This is not appropriate because as the wall-nozzle separation distance decreases, the adverse

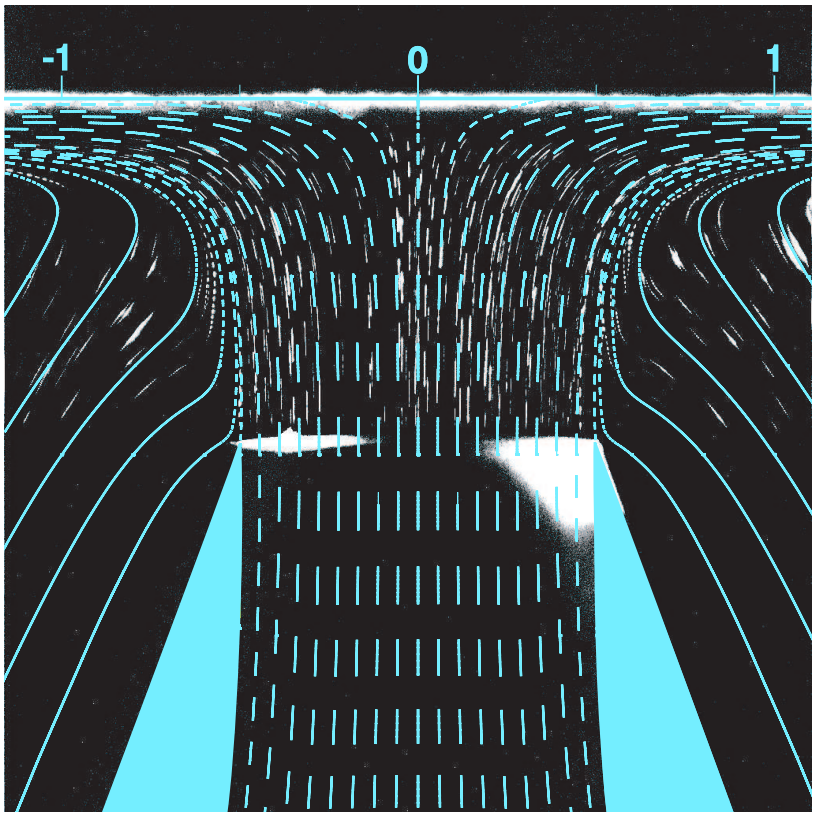

Figure 4.3: Particle streak image (monochrome) detailing entrained flow with superimposed axisymmetric viscous calculation (blue lines) at $Re = 700$ and $L/d = 1.0$

pressure gradient created by the stagnation point propagates upstream, inside the nozzle, and the exit axial velocity tends to have a larger velocity deficit. We term this the "wall-nozzle proximity effect" in this study. For large separation distances of $L/d > 1$, $u_0 \sim u_B$, however for smaller cases, say $L/d < 1$, as often employed to approximate idealized stagnation flow, u_0 is measurably smaller than u_B.

Fig. 4.3 compares particle-streak-image data and streamlines from the axisymmetric viscous simulations along the centerline. Good qualitative agreement can be seen, even in the entrainment region where the velocities are low ($< 0.02\, u_B$).

Fig. 4.4 shows axisymmetric simulation results on top of experimental data from (Bergthorson *et al.*, 2005a) at Re =400, 700, and 1400, respectively, for $L/d = 1.4$, which is the largest separation distance studied in Bergthorson *et al.* (2005a). All velocity data are taken along the axis and normalized by the Bernoulli velocity, u_B.

Although the code has gone through extensive verification processes, this cold flow simulation provides another layer of testing as the incompressible Navier-Stokes equa-

tions are regarded as a high-fidelity model of uniform-density flow. Within the range of Reynolds numbers studied, simulation and experiments are in good agreement. In many cases, the root-mean-square error of experimental data against numerical solution, which is a piecewise-smooth polynomial, is less than one percent of the reference velocity. Even the largest error was within 1.5%. Provided computed data contain rounding errors only, the small scatter in the experimental data are useful for the validation of chemical kinetics models that will be discussed in the next section.

When the ratio of the wall-to-nozzle separation distance to the nozzle diameter, L/d, is varied from 1.4 to 0.5, axial velocity profiles fall on top of a single curve when scaled by Bernoulli velocity. This is consistent with the finding reported in Bergthorson *et al.* (2005a). Fig. 4.5 gives pressure contours at $L/d = 0.5$ and 1.4, with pressures scaled by the Bernoulli pressure, which is the pressure drop across the nozzle. The near-wall pressure field is not significantly altered by changes in the nozzle position, and this fact explains the Bernoulli velocity scaling.

4.1.2.2 Assessment of the one-dimensional model

Although the one-dimensional model by Kee *et al.* (1988) was designed for axisymmetric stagnation flames, it also applies to nonreacting flow. In this case, the only equation to solve is the radial momentum equation, Eqn.(2.7), which is a third-order nonlinear ordinary differential equation. The one-dimensional model is based on a constant-pressure-eigenvalue assumption. The numerical evidence of the variation of the pressure eigenvalue is shown in Fig. 4.6. Although the variation in the radial direction is not significant, the profile shows nonuniformity in the axial direction. The profile is close to zero around the nozzle exit, if there is enough separation between the nozzle lip and the wall, but has an observable variation in the stagnating-jet region.

Fig. 4.7 compares the two-dimensional simulation velocity data, at $Re = 700$, to four different one-dimensional simulations, with plug-flow boundary conditions and different choices of the interior boundary location, ℓ. Solutions with plug-flow boundary conditions do not agree with the two-dimensional simulation data at any ℓ/d. When $\ell/d \geq 1.0$, the plug-flow (no velocity gradient) assumption provides a good approximation, as is evident from the figure where the very begining of the one-dimensional results agree with the two-dimensional data. However, one-dimensional solutions soon underpredict the axial velocity.

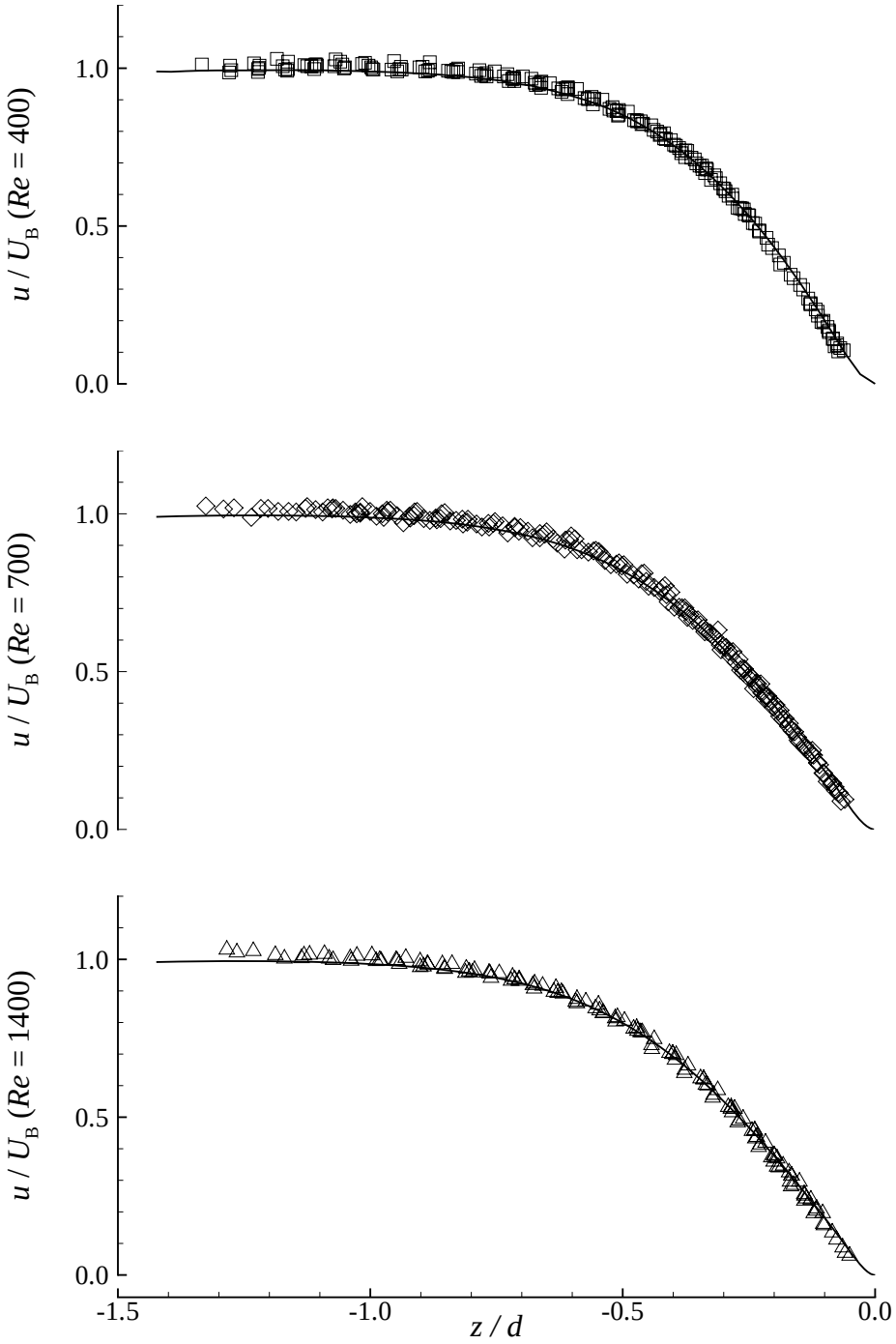

Figure 4.4: Axial velocity profiles along the axis of symmetry for $Re = 400$ (top), $Re = 700$ (middle), and $Re = 1400$ (bottom) with nozzle lip located at $z/d = -1.414$. Solid lines indicate two-dimensional simulations, while symbols indicate laboratory measurements by J. Bergthorson.

On the other hand, when $\ell/d \leq 0.8$, finite velocity gradients are evident and the plug-flow boundary condition is incorrect. In this case, the one-dimensional model tends to

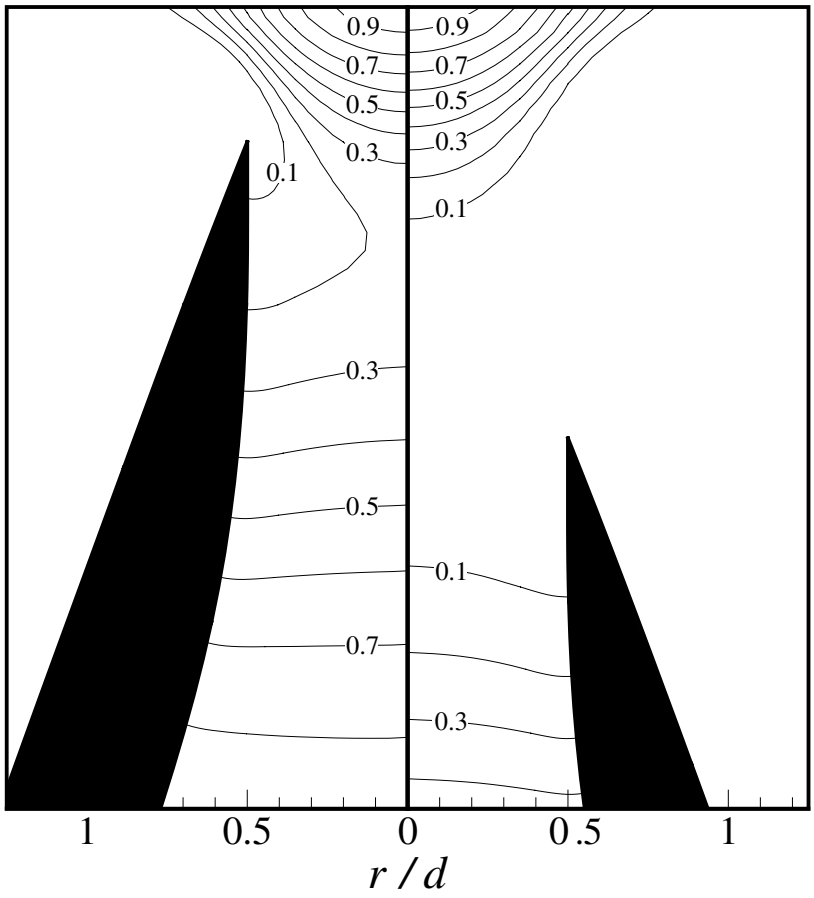

Figure 4.5: Pressure isocontours normalized by Bernoulli pressure at $L/d = 0.5$ (left) and $L/d = 1.4$ (right). (From Bergthorson *et al.*, 2005a)

overpredict soon after from the left boundary to the right boundary.

This is because the outer solution to the one-dimensional cold-flow equations is a parabola, as pointed by Davis *et al.* (2002b), which is a consequence of the uniform-eigenvalue assumption, and cannot capture the free-jet behavior (zero-gradient region of flow) exhibited for $z/d > 1.0$. However, this is the only questionable assumption in the one-dimensional model, and if $\Lambda(z)$ could be modeled or provided to the model by any means, the one-dimensional model should be able to predict flow fields along the axis well.

Since the plug-flow boundary condition works for no single case, a different boundary condition must be used for a one-dimensional model to be useful. The velocity and velocity-gradient boundary conditions at a given axial location, $U(\ell)$ and $U'(\ell)$, can be specified from a fitting function to the two-dimensional simulation data or the experimental data [see Eq. (4.3)], as described in Bergthorson *et al.* (2005a) and briefly discussed below.

The one-dimensional solution calculated using this method at $Re = 700$, over the range $0.3 \leq \ell/d \leq 0.7$, has a maximum error of less than 3% of u_{B} when compared to two-dimensional simulations.

4.1.2.3 Scaling parameters and error-function axial velocity profile model

As expected, for the flows investigated, Reynolds number is found to be a relatively weak parameter. Fig. 4.8 shows the maximum centerline axial velocity-gradient decreasing with increasing Reynolds number when scaled in this manner. The main effect of Reynolds number is the change in the effective jet diameter as a consequence of the boundary-layer displacement thickness. When u/u_{B} is plotted versus z/d_*, where d_* is the diameter corrected for nozzle-wall displacement thickness, the data collapse for all Reynolds numbers (Fig. 4.9) indicating minimal viscous effects in the free flow in the range of Reynolds numbers investigated. It is interesting to point out that this discovery was inspired by results of simulations without the nozzle-plenum assembly, *i.e.*, the inflow boundary conditions specified at the nozzle exit.

Kostiuk *et al.* (1993), in their study of turbulent jets, showed that opposed- or impinging-jet velocity data are well-characterized by an error function and used the parameters obtained from the error-function fit to collapse their experimental data. Their error function contained three adjustable parameters, the velocity at infinity U_∞, a strain-rate parameter α, and a wall-offset length δ/d,

$$\frac{u(z)}{U_\infty} \;=\; \mathrm{erf}\left[\,\alpha\,\left(\frac{z}{d} \,-\, \frac{\delta}{d}\right)\right] \;. \tag{4.3}$$

The collapse of the experimental and numerical data discussed above suggests that the appropriate velocity scale for laminar impinging jets is the Bernoulli velocity, *i.e.*, $U_\infty = u_{\mathrm{B}}$ as described in Bergthorson (2005) and Bergthorson *et al.* (2005a). From one-dimensional viscous stagnation-flow theory (see Bergthorson *et al.*, 2005a), the scaled-offset length, δ/d, which is proportional to the scaled wall boundary-layer thickness, can be related to the strain-rate parameter α, such that,

$$\frac{\delta}{d}(Re, \alpha) \;=\; 0.755\sqrt{\frac{1}{Re\,\alpha}} \;. \tag{4.4}$$

Thus, the only free parameter in this error-function fit to the data is the strain-rate parameter α, which should be a function of Reynolds number alone, *i.e.*, $\alpha = \alpha(Re)$. Therefore, the axial velocity field for an axisymmetric impinging laminar jet is fully specified by the Bernoulli velocity u_{B}, since the Reynolds number is, in turn, derived from it (Bergthorson *et al.*, 2005a).

The error-function fit to the numerical data at $Re = 1400$ is plotted in Fig. 4.10. The error function was fit to each experimental and simulation case by adjusting α such that the root-mean-squared (rms) error was minimized. For each Reynolds number, the strain-rate parameter α was averaged over the range $0.7 \leq L/d \leq 1.4$. This single $\alpha(Re)$ dependence was subsequently used in all error-function fits to determine the resulting rms error ϵ_{rms}. The fit parameters and ϵ_{rms} are shown in Table 4.1.

Table 4.1: Error-function fit parameters and rms error ϵ_{rms} of fits to experimental and viscous-simulation data.

			Experiment	Simulation
Re	α	δ/d	$\epsilon_{\mathrm{rms}}/u_{\mathrm{B}}$	$\epsilon_{\mathrm{rms}}/u_{\mathrm{B}}$
400	2.21	0.027	0.017	0.014
700	2.00	0.020	0.010	0.009
1400	1.88	0.015	0.011	0.010

This is very useful for determining suitable boundary conditions for one-dimensional simulations. Specifying the Bernoulli velocity, the Reynolds number is known and the strain-rate parameter, α, can be determined from Table 4.1. δ/d can be calculated from Eqn.(4.4). The analytical expression given by Eqn.(4.3) can be used to calculate the velocity profile along the axis.

4.1.2.4 Effect of nozzle design for stagnation-flow experiments

As previously mentioned, the main Reynolds number effect for this flow is through the nozzle-wall boundary-layer thickness. The effect of the nozzle-exit velocity profile is studied in Fig. 4.11 for profiles varying from a top-hat shape, representative of the outflow from a high-contraction ratio nozzle, to a parabolic profile, representative of fully developed laminar pipe flow. Real nozzle-exit velocity profiles should lie between these two extremes. Intermediate cases are studied by specifying hyperbolic tangent profiles whose coefficients are adjusted to represent the variation of boundary-layer displacement-thicknesses. The results in Figs. 4.11 and 4.12 are obtained by removing the nozzle interior from the axisym-

metric two-dimensional simulation domain and specifying the velocity profiles at the nozzle exit. Due to the lack of a plenum in the simulations, velocities are scaled by the velocity at the axis of the jet, u_0, instead of the Bernoulli velocity. Fig. 4.11 indicates that there is a significant effect of the nozzle-exit velocity profile on the resultant axial velocity field. Fig. 4.12 plots the axial velocity profiles with the axial distance normalized by the effective diameter d_*, which is the boundary-layer thickness corrected diamter. For $d_*/d > 0.9$ this scaling results in a good collapse of the profiles.

Fig. 4.11 also shows the importance of appropriate modeling when comparing to experimental data, in particular for model validation. It is a simple task to adjust boundary conditions such that numerical simulations and experimental data coincide given such a wide variation in the velocity profile—if 'validation' is conducted inappropriately without modeling the important details of the experimental setup.

4.1.3 Summary

Good qualitative and quantitative agreement is observed between laboratory measurements and the simulation of corresponding laboratory phenomena. Both simulation and measurements provide accurate velocity profiles along the axis. In addition to comparisons along the axis, a comparison of streamlines and particle streaks provides other criteria. Based on these simulation data and experimental data, a new error function model on the axial velocity was obtained that describes axial velocity profile at range of Reynolds numbers and plate-nozzle separations uniformly. In contrast, the one-dimensional model disagrees with the experimental data and the two-dimensional simulation data if a plug-flow boundary condition is employed. However, since the error function describes the axial flow field well enough, it is possible to use it to supply an approximate boundary condition to the one-dimensional model as follows:

1. Carry out a series of 2D simulations to determine the nozzle characteristics used in the experiment and obtain Re-d^* relations.

2. Use the error-function fit to determine the centerline velocity profile.

3. Use the fit to obtain the boundary conditions for 1D model.

4. Conduct the 1D simulation.

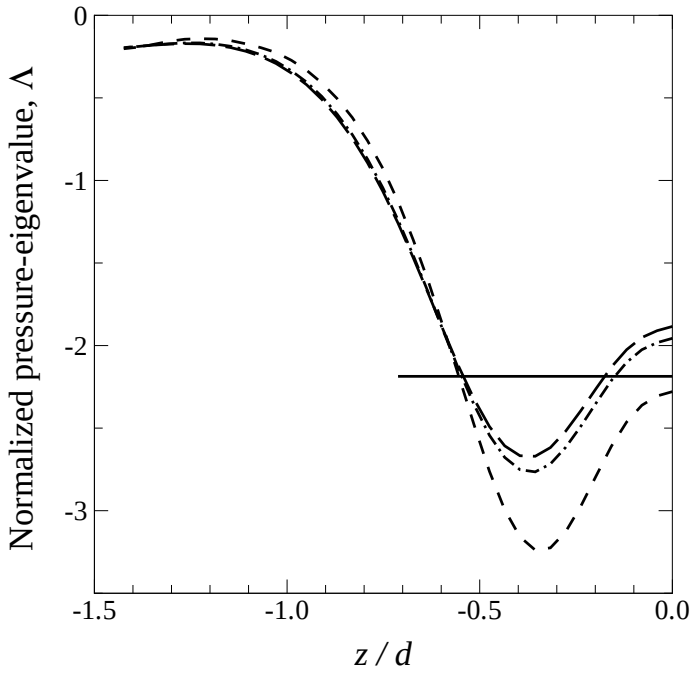

Figure 4.6: Comparison of the radial-pressure eigenvalue profile at several radial locations, $r/R = 0$ (long-dashed line), $z/R = 0.2$ (dash-dotted line), and $r/R = 0.5$ (dashed line), to that of the one-dimensional model (solid line), which is constant in both z and r.

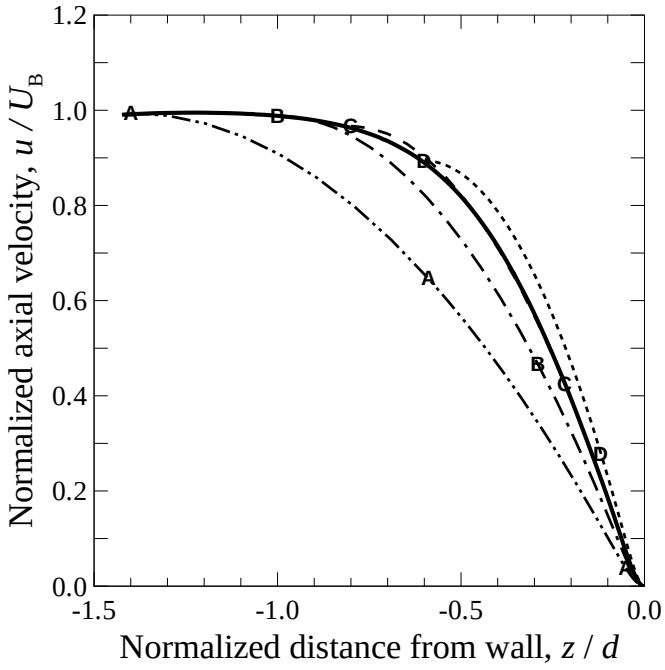

Figure 4.7: Comparison of one-dimensional numerical results with plug-flow boundary conditions with varying l/d: 1.4 (A), 1.0 (B), 0.8 (C), and 0.6 (D). The two-dimensional numerical result is shown as a reference. Plug-flow boundary conditions cannot predict the axial velocity profile at any separation distance. Although the two-dimensional result shows the velocity gradient is nearly zero at $z/d = 1.4$, the one-dimensional model cannot follow the trajectory of the two-dimensional simulation result. This is a manifestation of the uniform pressure eigenvalue assumption.

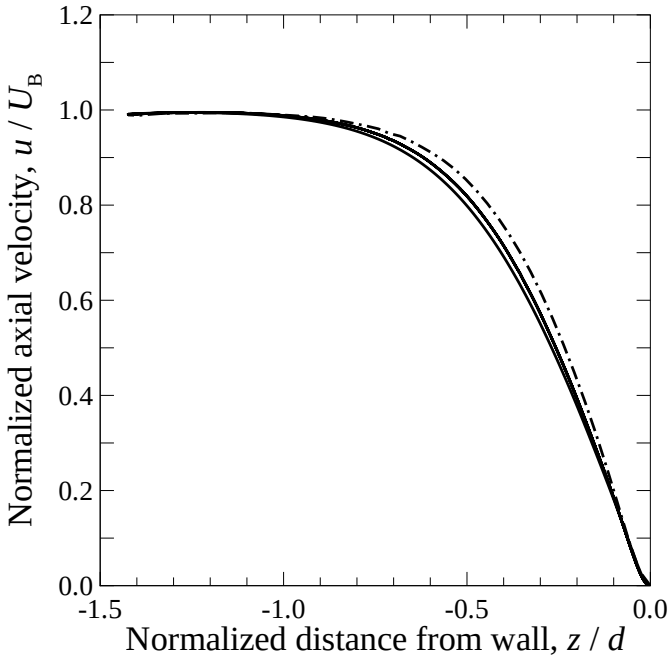

Figure 4.8: Axial velocity profiles from two-dimensional simulations versus axial distance from plate normalized by the nozzle diameter d at $L/d = 1.4$ and Re =400 (dash-dotted line), 700 (dotted line), and 1400 (solid line)

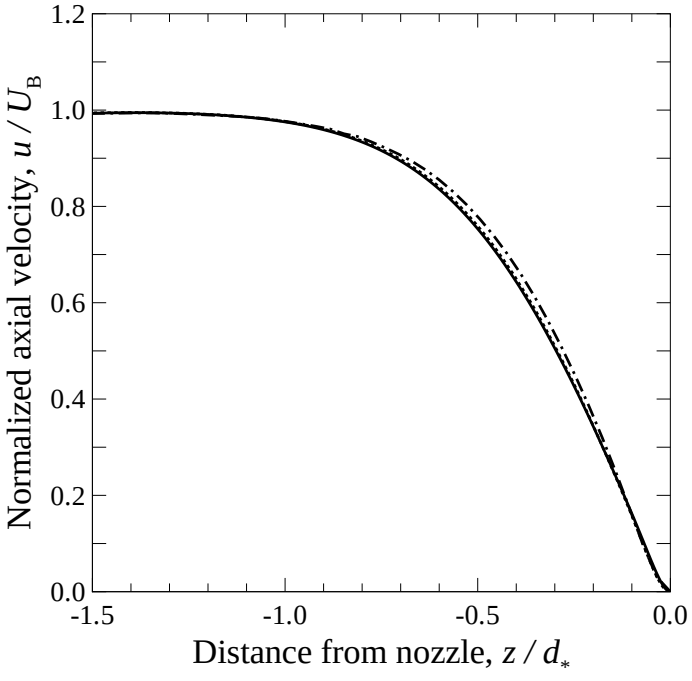

Figure 4.9: Two-dimensional simulation velocity profiles versus axial distance from the plate, normalized by the effective diameter d_* at L/d=1.4 and Re=200 (long-dashed line), 400 (dash-dotted line), 700 (dotted line), and 1400 (solid line)

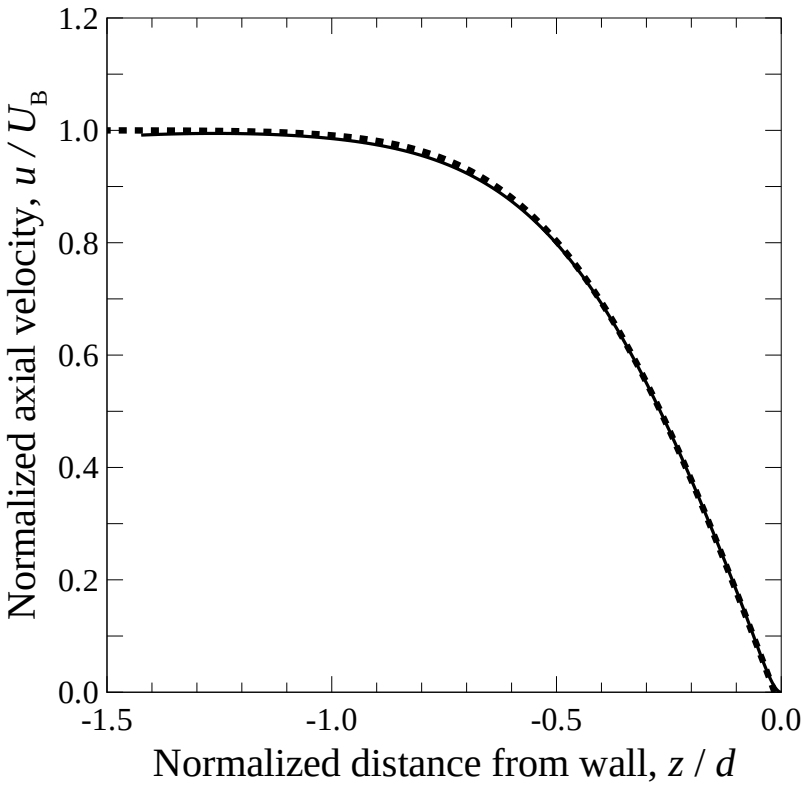

Figure 4.10: Comparison of error-function fit (dotted line) to two-dimensional simulation data (solid line) at $Re = 1400$

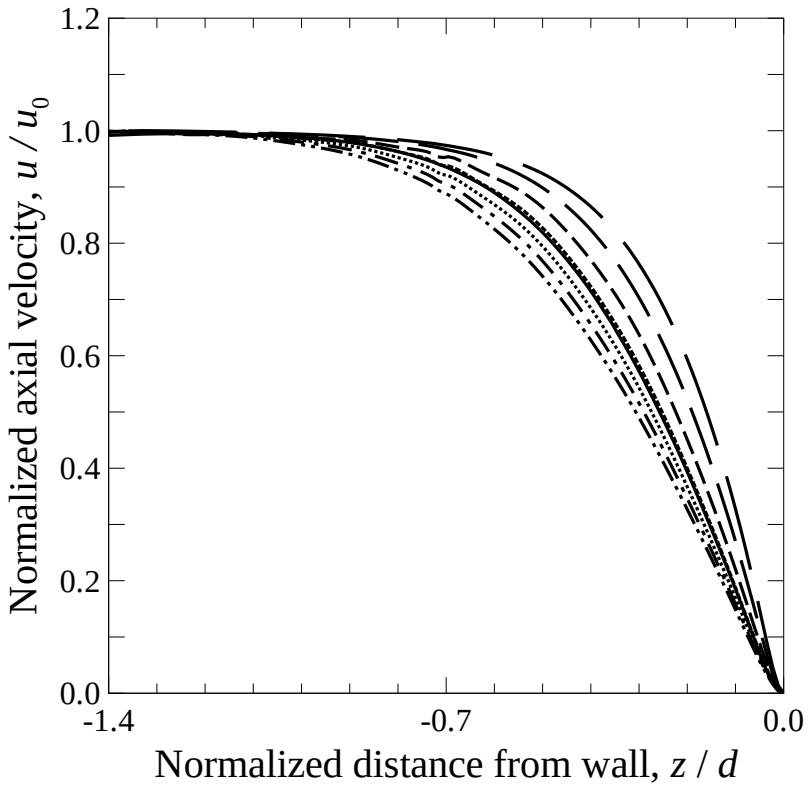

Figure 4.11: Simulated velocity profiles at $Re = 700$ and $L/d = 1.4$ for variable nozzle-exit velocity profiles: Parabolic ($d_*/d = 0.71$, long dash), hyperbolic-tangent profiles with $d_*/d = 0.76$ (medium dash), $d_*/d = 0.82$ (dash), $d_*/d = 0.87$ (short dash), $d_*/d = 0.91$ (dot), $d_*/d = 0.95$ (dash-dot), and top-hat ($d_*/d = 1.0$, dash-dot-dot) profiles. Simulation with nozzle at the same condition is plotted with a solid line, indicating that the nozzle used in the experiments by Bergthorson *et al.* (2005a) and Bergthorson (2005) produces $0.87 < d_*/d < 0.91$.

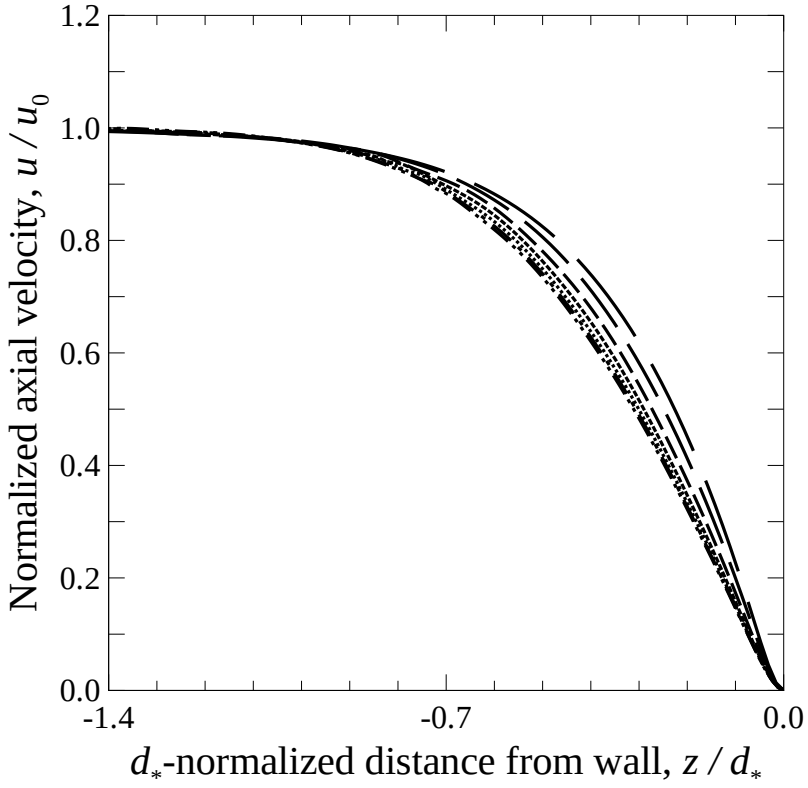

Figure 4.12: Simulated velocity profiles versus axial distance from the plate, normalized by the effective diameter d_* at $Re = 700$ and $L/d = 1.4$, for variable nozzle-exit velocity profiles. The last four curves are now nearly indistinguishable, indicating the benefit of a high contraction area-ratio nozzle. (Legend are as in Fig. 4.11.)

4.2 Steady stagnation flames

4.2.1 Introduction

When the flow supports chemical reactions, the details of each reaction must be modeled. There is more than one model for hydrocarbon combustion available. Perhaps the most widely accepted model of methane combustion is GRI-Mech 3.0. Although methane is the simplest hydrocarbon and its combustion is relatively well understood among hydrocarbon fuels, there are still uncertainties and modeling its chemical kinetics is far from satisfactory, mostly because of the large number of reactions involved. For example, GRI-Mech 3.0, less nitrogen reactions (model HC1 in Table 1.1), features 217 reactions, whereas its hydrogen reaction subset contains only 28 reactions.

Although widely used, these reaction mechanisms have not been completely validated. A realistic simulation of a laboratory flame has been computationally expensive and validation attempts have been difficult. Therefore simulations of hydrocarbon flames reported to date can be categorized into two types: ones that employ full chemical kinetics models such as GRI-Mech 3.0 along with a one-dimensional fluid mechanical model proposed by (Kee *et al.*, 1988), and ones that use a multi-dimensional Navier-Stokes model of fluid mechanics with a reduced chemistry model (Smooke *et al.*, 1986, 1992). For example, Egolfopoulos (1994) used one-dimensional model and the EDL92 mechanism (see Table 1.1) to study radiation effects in an opposed-jet premixed and non-premixed flames. To the author's knowledge, no multi-dimensional simulations of hydrocarbon stagnation or opposed-jet flames were reported, however, there are several multi-dimensional simulations of laminar hydrocarbon flames. Bennett *et al.* (1999) simulated a steady axisymmetric Bunsen flame using GRI-Mech 1.2 (HC2 in Table 1.1). Regardless of the type of problems, many kinetic mechanisms have been studied mostly within the context of the one-dimensional hydrodynamic model, with numerical results subsequently compared to experiments. Of course, the fluid mechanical part of the one-dimensional model is also approximate, as was shown in the case of cold flow, and comparisons within such a oversimplified framework can be misleading.

As explained earlier, an efficient algorithm has been developed to simulate hydrocarbon flames in this study. To further reduce computational time required before the simulated flame reaches to the steady state, the simulations are conducted in three phases. Phase I relies on the one-dimensional simulation using Cantera. This provides an approximate flame

location, as well as desired mesh distribution so that the Phase II computational domain can have a cluster of elements near that region. In addition, it provides a good initial condition to the Phase II simulation, as described in Appendix B. The Phase II simulation is the axisymmetric two-dimensional simulation with a truncated domain. The computational domain contains a stagnation region and some of the post-flame and entrainment regions only. No nozzle-wall proximity effect is considered in this case. All Phasse II computations reported in the present study are recorded in Table 4.2. Finally, Phase III is the "real" simulation that contains the interior of the nozzle and the enclosure of the nozzle-wall assembly, within which nozzle-wall proximity effects as well as entrainment is appropriately captured in the simulation, and models the experiments documented by Bergthorson *et al.* (2005b), Bergthorson & Dimotakis (2007), and Bergthorson (2005). All Phase III simulations are recorded in Table 4.3.

All reacting flow simulations reported in this study have a unique case number. The first character signifies the type of the domain: A for 1-D model, B for 2-D Phase II model, and C for 2-D Phase III model, followed by three-digit numbers that corresponds to the equivalence ratio—070 should read $\Phi = 0.70$. The number after the dash is a unique identification number among each setup. All simulations reported in this study use the GRI-Mech 3.0 model, less nitrogen reactions (model HC1 in Table 1.1). It was confirmed independently that the nitrogen chemistry do not alter the numerical results by comparing one-dimensional results using the HC1 and HCN1 mechanisms in Table 1.1.

In their study of laminar flame speed, Wu & Law (1984) suggested the use of stretched flames to determine the laminar flame speed in the limit of flame stretch going to zero and demonstrated the use of stagnation flames for this purpose. Since then, this extrapolation-based laminar flame speed determination has been commonly used. Later Tien & Matalon (1991) showed that the flame-stretch to flame-speed relationship can vary depending on how reference locations are selected, and they resolved inconsistency and confusion in the literature about how to extrapolate to obtain laminar flame speed. Such extrapolated laminar flame speeds are reported, for example, in Egolfopoulos *et al.* (1997), Dong *et al.* (2002), and Hirasawa *et al.* (2002), and comparisons between experimentally determined laminar flame speed (through extrapolation) and simulation of freely propagating flame (using 1-D codes such as CHEMKIN / PREMIX) have been made. Bergthorson *et al.* (2005b) were probably the first to attempt estimates of modeling errors in GRI-Mech 3.0

Table 4.2: Phase II simulation data. (See page 78 for the definitions of symbols.)

Case	Φ	σ (1/s)	Γ (1/s)	$S_{\mathrm{u,ref}}$ (m/s)	z_{Flame} (m)	κ (1/m)	Figure
B070-2	0.70	67.01	118.80	0.241709	-0.004353	184	C.1
B070-7	0.70	82.25	111.69	0.242096	-0.003941	114	C.2
B070-12	0.70	97.80	107.24	0.2437	-0.003650	77	C.3
B070-17	0.70	111.79	107.91	0.2454	-0.003360	48	C.4
B070-22	0.70	123.22	114.36	0.2471	-0.003100	44	C.5
B070-27	0.70	135.84	119.80	0.2479	-0.002836	16	C.6
B070-30	0.70	142.67	124.37	0.2476	-0.002681	13	C.7
B080-17	0.80	136.98	138.32	0.3212	-0.004047		C.8
B080-46	0.80	223.46	178.60	0.3346	-0.002769		C.9
B090-35	0.90	184.13	173.83	0.3820	-0.003966	30	C.10
B090-50	0.90	296.77	228.21	0.3942	-0.002695	13	C.11
B090-106	0.90	342.38	258.72	0.3989	-0.002322	8	C.12
B090-112	0.90	406.32	312.93	0.4015	-0.001855	4	C.13
B100-23	1.00	228.38	200.92	0.4201	-0.003740		C.14
B120-10	1.20	171.81	189.01	0.3707	-0.003760	43	C.15

Table 4.3: Phase III simulation data. (See page 78 for the definitions of symbols.)

Case	Φ	σ (1/s)	Γ (1/s)	$S_{\mathrm{u,ref}}$ (m/s)	z_{Flame} (m)	κ (1/m)	Figure
C070-4	0.70	104.01	67.62	0.2365	-0.004421	-49	C.16
C070-11	0.70	112.20	71.20	0.2386	-0.004133	-55	C.17
C070-8	0.70	115.91	73.46	0.2395	-0.003997	-56	C.18
C070-9	0.70	127.60	81.19	0.2423	-0.003633	-59	C.19
C090-5	0.90	209.33	89.76	0.3734	-0.004936	-44	C.20
C090-2	0.90	238.55	116.42	0.3819	-0.004224	-37	C.21
C090-4	0.90	246.01	122.25	0.3848	-0.004103	-31	C.22
C090-3	0.90	253.51	128.79	0.3862	-0.003952	-30	C.23
C120-1	1.20	229.77	126.68	0.3512	-0.003694	-29	C.24

without extrapolating to a stretch-free state. In their approach, instead of flame speed, flame location was used as a surrogate for flame strength, and they studied flames at different equivalence ratios using appropriate dilutions to allow the flame to be realized at about the same strain rate.

Although in their original paper, Wu & Law (1984) used the word 'stretch,' what they used as a measure of flame stretch was a strain-rate (normal strain) upstream of the flame where the effect of heat release is minimal. Flame stretch, as defined later, will be accepted as representing a lateral-strain rather than normal-strain. Because in the case of idealistic

potential flow solution of stagnation flow, strain and stretch are related and differ only by a factor of two (Law & Sung, 2000), if measured at the same location and dilatation is excluded. This seems to be the cause of mixed use about 'stretch' and 'strain' in the literature when, in many cases, both terms mean the same quantity—a flame-normal strain-rate, $\mathbf{n} \cdot \nabla \mathbf{u} \cdot \mathbf{n}$, where $\mathbf{n}$ is a normal vector of a flame front. Of course, when defined at the same location, strain and stretch are related through the continuity equation. For example, along the axis, $\sigma_n + 2\sigma_t = -\partial\rho/\partial z$ where $\sigma_n = \partial u/\partial z$ and $\sigma_t = \partial v/\partial r$

4.2.2 Results and discussion

4.2.2.1 Validation of the one-dimensional model

The uniform-pressure eigenvalue assumption and the inappropriateness of plug-flow boundary conditions were shown to lead to erroneous results for the cold flow case. The behavior of the same one-dimensional model when chemical reactions are present is investigated here. The computational domain used for this study is shown in Fig. 4.13. The one-dimensional numerical solution for the same separation distance at the same flow condition is obtained *a priori* for each two-dimensional simulation, and the solution is extrapolated in the radial direction to obtain an initial condition to the two-dimensional model (see Appendix B). The inflow velocity condition, as well as the entrainment flux, is specified at the nozzle exit. The wall is isothermal and kept to $T_{\text{wall}} = 300\,\text{K}$ throughout the study. The outflow boundary condition is applied at the outermost boundary at $r = 2.0\,\text{cm}$. In the following analysis, velocity and other quantifies are plotted only along the axis unless otherwise noted.

Shown in Fig. 4.14 is an axial velocity profile comparison along the axis between the two-dimensional model and the one-dimensional model (Cantera), at the equivalence ratio of $\Phi = 0.70$. The velocity profile deviates as it approaches the flame when the plug-flow boundary condition is used, and there is a difference in the prediction of flame location between two-dimensional and one-dimensional models. This difference is attributable to the uniform pressure-eigenvalue assumption in the one-dimensional formulation. However, this can be overcome by specifying the boundary condition in the middle of the nozzle-flame proximity with the velocity boundary condition values taken directly from the two-dimensional simulation, as discussed by Bergthorson *et al.* (2005b) for comparisons between experiments and one-dimensional simulations, and as shown in Fig 4.15. (Hereafter, this

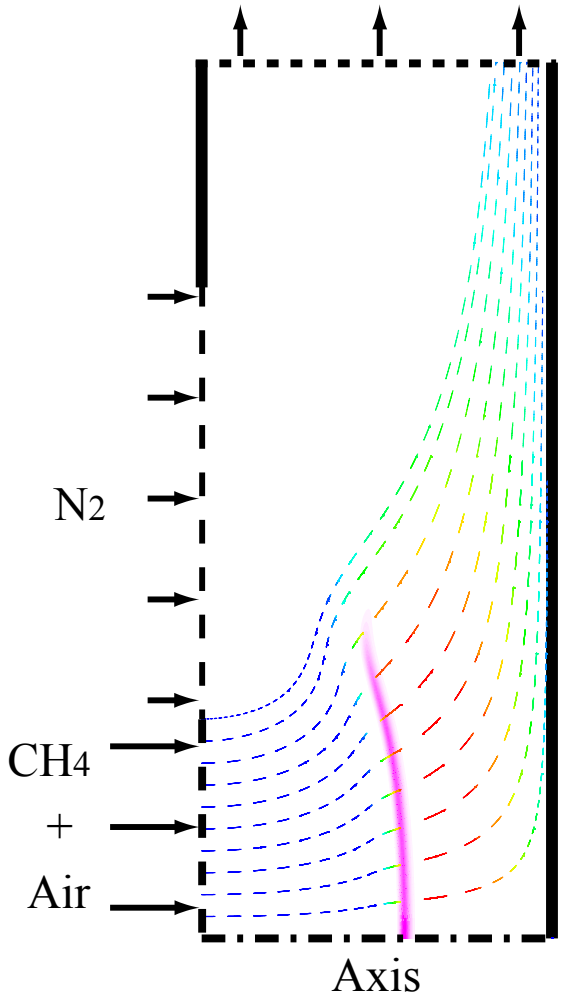

Figure 4.13: A computational domain used for the Phase II numerical studies and a typical realization of the flow field (streamlines shown as dashed lines), temperature field (color of the streamlines), and the flame (mass fraction of CH shown in pink). The actual allocation of elements within the domain varies for each case.

short domain case with a finite spreading rate boundary condition is denoted as 1D-s.) It indicates the plug-flow boundary condition cannot be used for any practical comparison with experimental data or multidimensional simulations, even when there is no velocity gradient at the nozzle exit, which is consistent with previous findings in the case of non-reacting flow (Bergthorson *et al.*, 2005a). To illustrate the discrepancy between two- and one-dimensional models, Fig. 4.16 presents the pressure-eigenvalue profiles. In one-dimensional models, this is assumed to be a constant, as indicated in the figure (dashed line). The pressure eigenvalue profile has a large spike near the flame front. This is in contrast to earlier hydrogen flame simulations reported by Frouzakis *et al.* (1998) and provides another reason that renders hydrocarbon flame simulation challenging. This spike is mainly because of the thinness of the flame as well as the curvature of the flame front. The magnitude of the pressure eigenvalue affects the prediction of the spreading rate, $V(= \partial v/\partial r)$, in the one-dimensional model and results in an overprediction or underprediction of the spreading rate in the near- and post-flame region, as shown in Fig. 4.17. On the other hand, the location and the size of the spike has no discernible effect on the prediction of flame location in the one-dimensional model, as shown in Fig. 4.15. This implies that the pressure eigenvalue profile between nozzle and the flame is an important factor in determining flame location, and must somehow be also accounted for in one-dimensional formulations, if high accuracy is of importance.

As the volume flux through the inlet boundary is increased, the flame moves close to the stagnation wall. The pressure-eigenvalue profile changes as the flame moves, as shown in Fig. 4.19. The depth of the spike reduces gradually as the flame moves to the wall. This is primarily because the flame loses its curvature as the strain-rate increases.

To discuss the flame behavior, let us define several important parameters about flames used in the present study: strain (σ), stretch (Γ), reference flame speed ($S_{\mathrm{u,ref}}$), location (z_{flame}), and curvature (κ). In this study, the flame is defined as a set of points that maximizes the mass fraction of CH along each streamline. Presently, analysis is conducted only along the axis, and therefore, z_{flame} is a point such that $Y_{\mathrm{CH}}(z_{\mathrm{flame}}, 0)$ is maximum along the axis. Strain-rate, σ, is defined by the maximum slope upstream of the flame, z_{flame}, which is an inflection point of axial velocity curve, whereas the reference flame speed is the local minimum velocity upstream of the flame. The flame stretch is a lateral strain at the flame front, $\partial v/\partial r(z_{\mathrm{flame}}, 0)$, and is defined more precisely later. These definitions

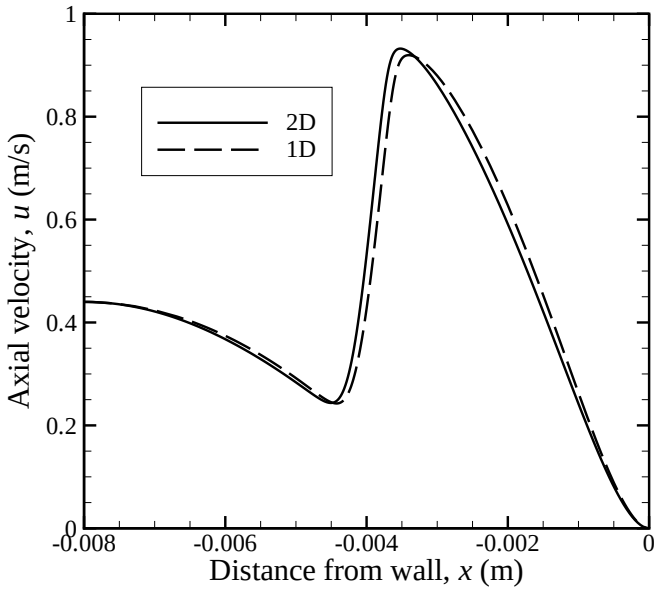

Figure 4.14: Comparison of two-dimensional and one-dimensional solutions with the plug-flow boundary conditions to one-dimensional model. Both models employ the same domain length (0.008 m) in the axial direction. Even with the same zero-slope boundary condition specified to both two- and one-dimensional models, the one-dimensional model fails to follow the axial velocity profile of the two-dimensional model.

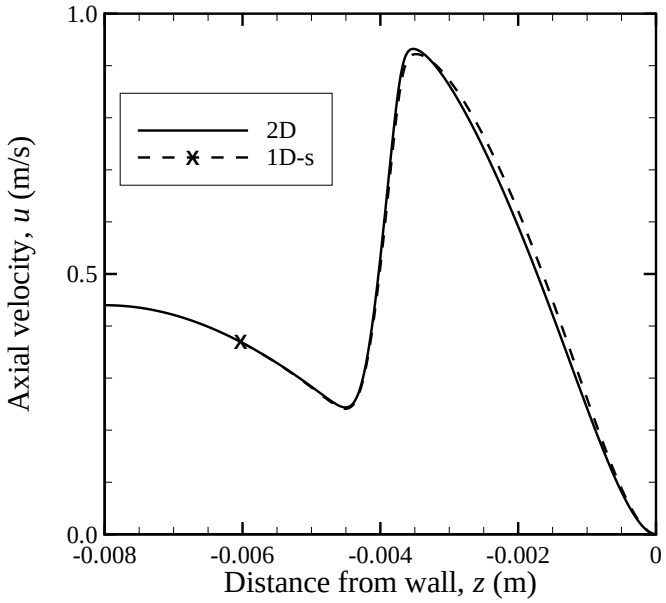

Figure 4.15: Comparison of two-dimensional and one-dimensional solutions with the boundary conditions to one-dimensional model specified at $z = -0.006$. Better agreement between the one-dimensional model and the two-dimensional model can be seen in this case, compared to the plug-flow boundary condition (Fig. 4.14).

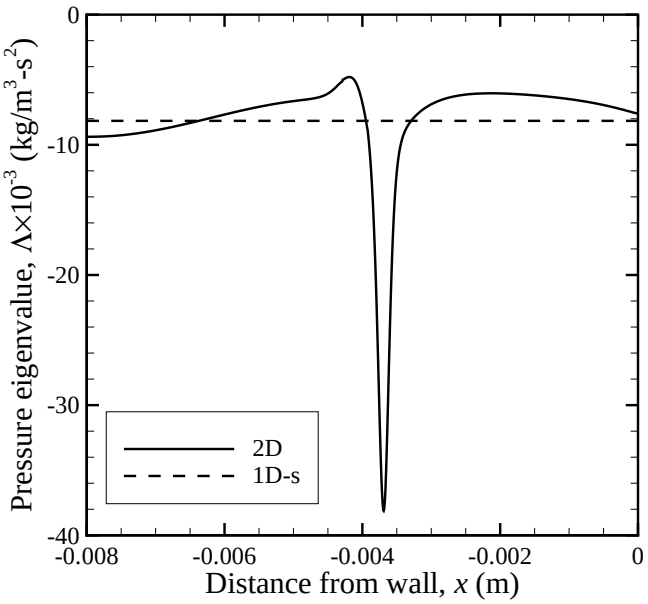

Figure 4.16: Pressure eigenvalue profile along the axis in a methane-air flame ($\Phi = 0.7$). Note the sharp spike at the flame front when the correct pressure field is obtained, which contrasts with a uniform profile assumed in the one-dimensional model. (Legend as shown within the plot.)

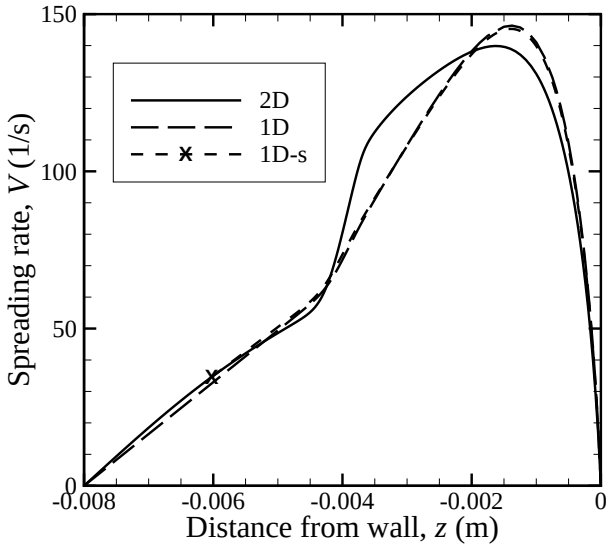

Figure 4.17: The spreading rate, $\partial v/\partial r$, profile along the axis in a methane-air flame ($\Phi = 0.7$). Within the reaction zone, the spreading rate changes, which is an effect that is not incorporated in the one-dimensional model as a consequence of the uniform pressure-eigenvalue assumption.

are schematically shown in Fig. 4.18. It should be pointed out, in this convention, the locations at which strain is defined and stretch is defined are different. The former is defined somewhere in the early part of preheat zone while the latter is defined at the flame front—within a thin reaction zone.

The local flame curvature on the symmetric axis can be written as,

$$\kappa = 2/\mathcal{R}_{\text{Flame}}, \tag{4.5}$$

where $\mathcal{R}_{\text{Flame}}$ is the radius of curvature of the flame front and is given by (Gray, 1997)

$$\frac{1}{\mathcal{R}_{\text{Flame}}} = \frac{g_{zz}g_r^2 - 2g_{zr}g_z g_r + g_{rr}g_z^2}{(g_z^2 + g_r^2)^{3/2}}, \tag{4.6}$$

where $g(z,r) = 0$ defines the flame front and subscripts denote its derivatives in the above expression. Since the CH radical is used as a marker in the present study, $g(z,r) \equiv \partial Y_{\text{CH}}/\partial z$ can be used. Furthermore, $g_r = 0$ along the axis. This simplifies the expression for curvature to:

$$\kappa = 2\frac{g_{rr}}{g_z}. \tag{4.7}$$

The factor of two is because of the azimuthal symmetry (*e.g.*, Candel & Poinsot, 1990) for axisymmetric flames.

Curvature is positive when the flame is concave toward the unburnt gas and negative when the flame is convex toward the unburnt gas. Phase II simulations always produced positively curved flames. The shapes and the curvature of flames at various conditions can be observed in the flame-simulation data in Appendix C. When curvature is small, the one-dimensionl simulation with the slope-matched boundary condition (1D-s) works well, as shown in Figs. 4.20 and 4.21. However, when flame curvature is large, even the 1D-s case does not follow the axial velocity profile obtained by two-dimensional simulation, as shown in Figs. 4.22 and 4.23. It is imperative to keep flame curvature as small as possible if a comparison to the one-dimensional model is to be meaningful.

Shown in Figs. 4.24 and 4.25 are the axial velocity and the spreading rate at the equivalence ratio of $\Phi = 0.90$. The profile for the $\Phi = 1.20$ case is plotted in Figs. 4.26 and 4.27. In both of these cases, the one-dimensional model predicts a stronger flame than is predicted by the two-dimensional model. The implications will be discussed later.

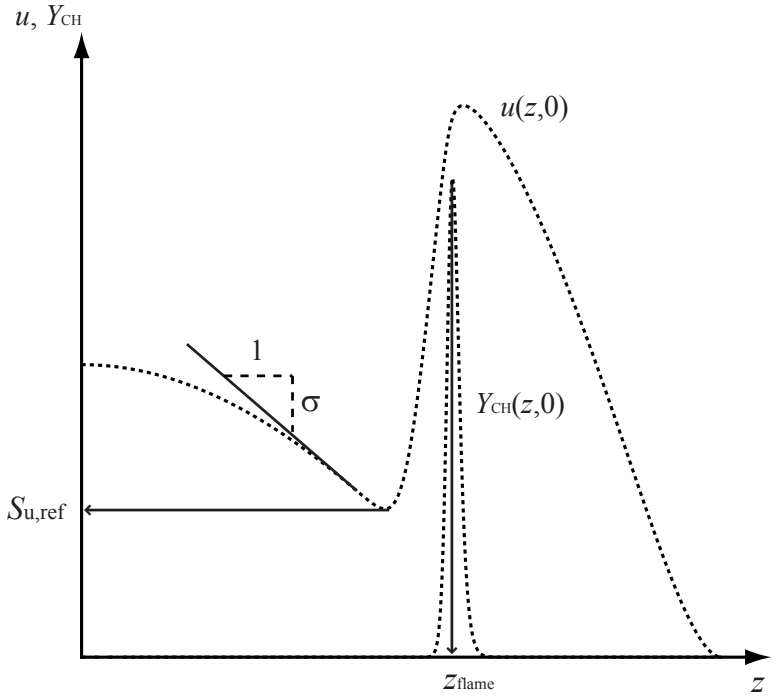

Figure 4.18: Definitions of some of important parameters describing flames: σ: strain-rate, $S_{\mathrm{u,ref}}$: Reference flame velocity, and z_{flame}: flame location are shown here. κ, flame curvature, and Γ, flame stretch, are defined at $z = z_{\mathrm{flame}}$ and $r = 0$.

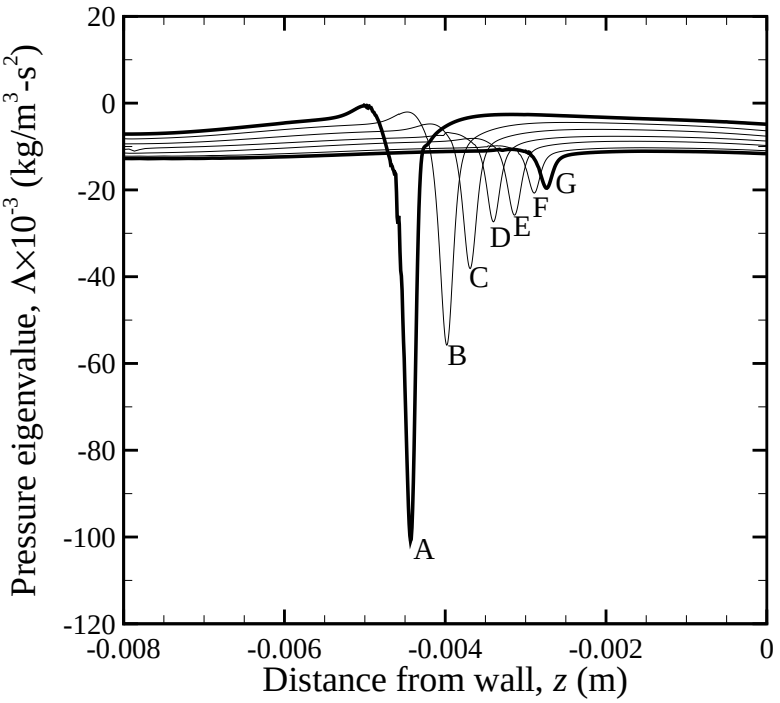

Figure 4.19: Variation of pressure-eigenvalue profile as flame strain-rate changes. Note the depth of the spike decreases gradually as the flame loses its curvature. (A): Case B070-2; (B): Case B070-7; (C): Case B070-12; (D): Case B070-17; (E): Case B070-22; (F): Case B070-27; (G): Case B070-30. See Table 4.2 for parameters for each case.

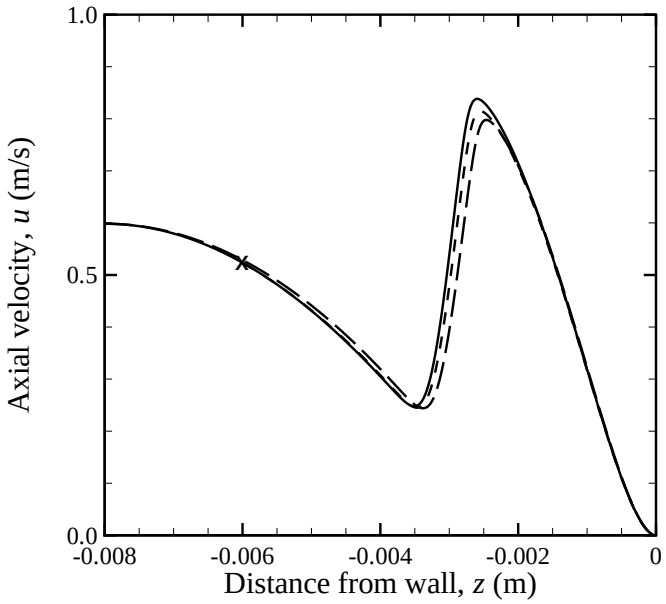

Figure 4.20: Comparison of the axial velocity profile between the one-dimensional model (Case A070-30) and the two-dimensional model (Case B070-30) using the same kinetics mechanism at $\Phi = 0.70$. In this case, the pressure-eigenvalue profile has the smallest peak in absolute value, and the difference between the one-dimensional model and the two-dimensional model is small. 2-D (solid line), 1-D with plug-flow BC (long dashed line), and 1-D with boundary conditions taken from 2-D simulation (short dashed line with X denoting the location where the boundary condition is specified)

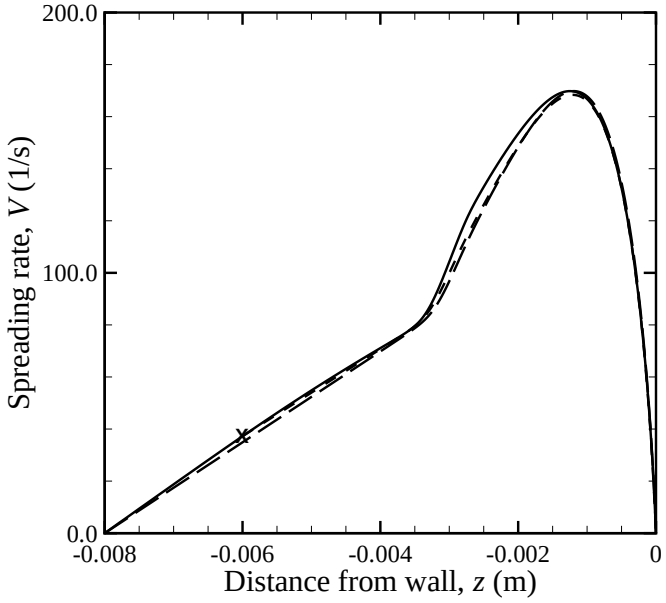

Figure 4.21: Comparison of the spreading rate (radial velocity gradient) profile between the one-dimensional model (Case A070-30) and the two-dimensional model (Case B070-30) using the same kinetics mechanism for $\Phi = 0.70$. Again, the difference is smaller compared to the earlier case when a large pressure eigenvalue led to a large discrepancy in the spreading rate. (Legend as in Fig. 4.20.)

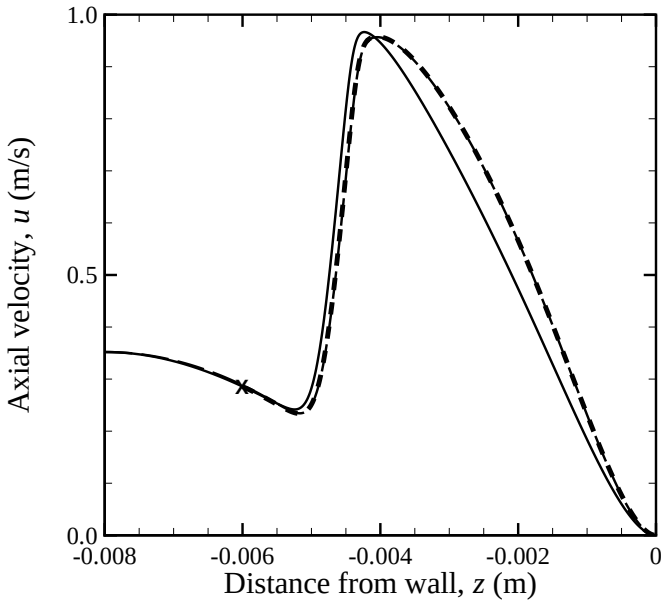

Figure 4.22: Comparison of two-dimensional (Case B070-2, solid) and one-dimensional (Case A070-2) solutions with two different boundary conditions: Plug-flow (short dash) and velocity-gradient specified with truncated domain (long dash). 'X' denotes the location where the boundary condition is specified for the truncated-domain case. This is the flame with the smallest strain-rate realized in this study. The equivalence ratio is 0.70. In this case, the flame is curved so strongly (see Fig. C.1 in Appendix C) that flame location cannot be predicted by the one-dimensional solution, even with the correct boundary conditions given by the two-dimensional solution.

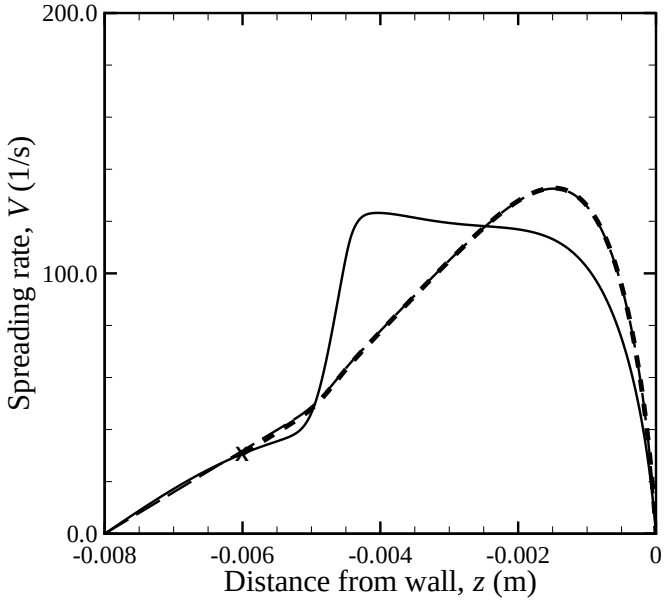

Figure 4.23: Comparison of the spreading rate, $V(= \partial v/\partial r)$, along the axis between two-dimensional (Case B070-2) and one-dimensional (Case A070-2) solutions. (Legend as in Fig. 4.22.)

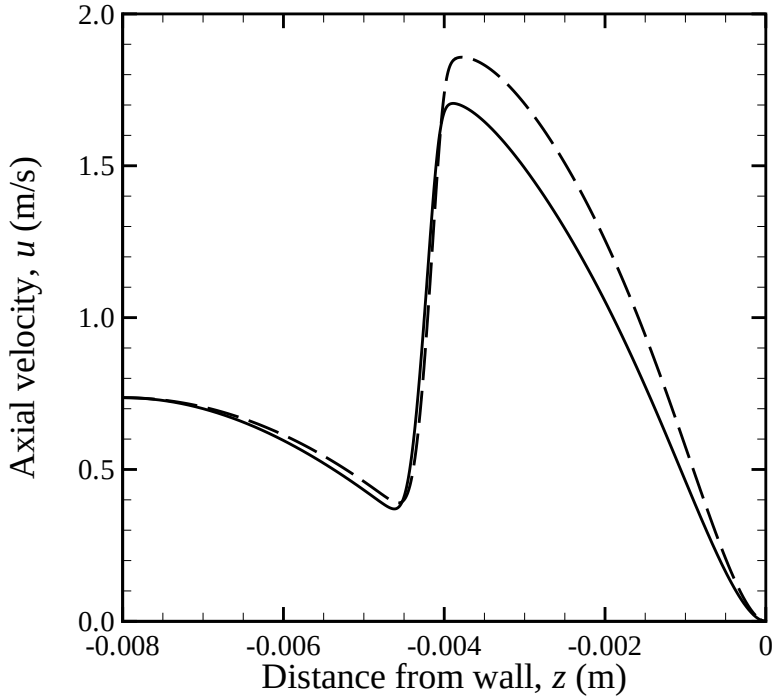

Figure 4.24: Comparison of the axial velocity profile between the two-dimensional model (Case B090-35) and the one-dimensional model (Case A090-35), using the same kinetics mechanism, for $\Phi = 0.90$. (Legend as in Fig. 4.20.)

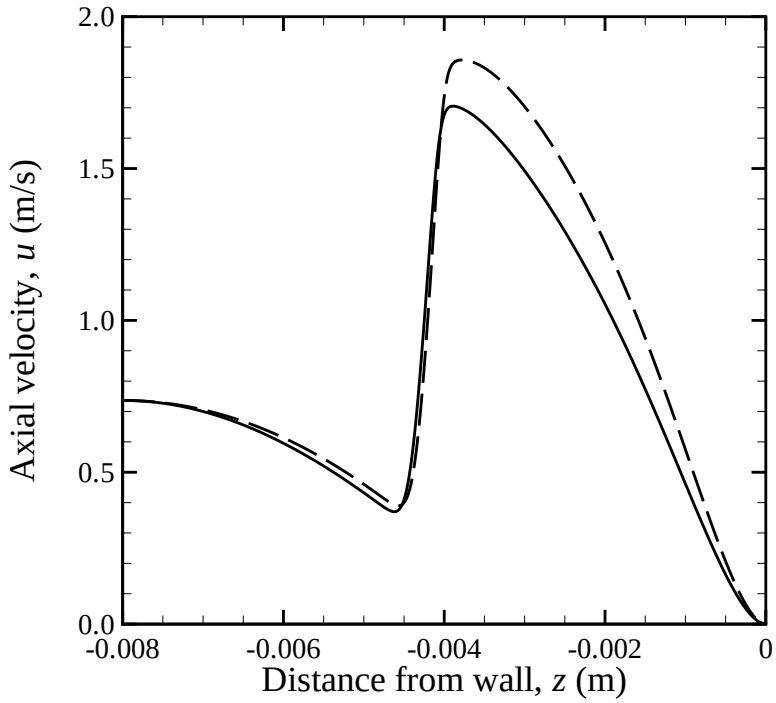

Figure 4.25: Comparison of the spreading rate (radial-velocity gradient) profile between the two-dimensional model (Case B090-35) and the one-dimensional model (Case A090-35), using the same kinetics mechanism, for $\Phi = 0.90$. (Legend as in Fig. 4.20.)

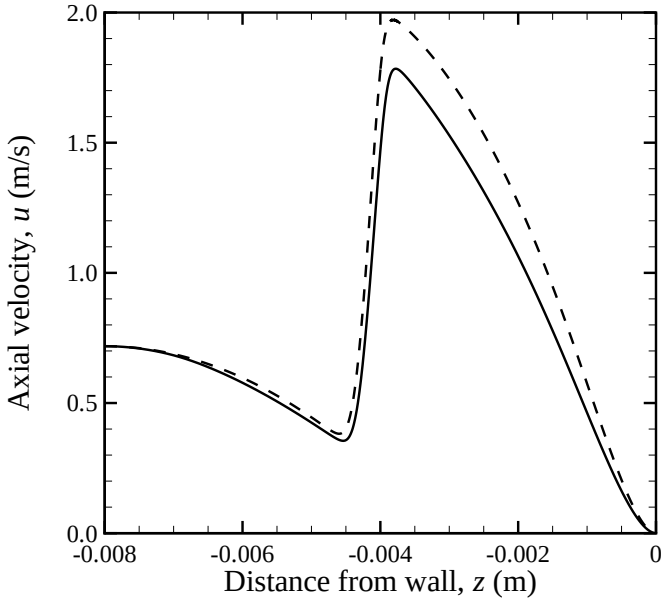

Figure 4.26: Comparison of the axial velocity profile between the two-dimensional model (Case B120-10) and the one-dimensional model (Case A120-10), using the same kinetics mechanism, for $\Phi = 1.20$. (Legend as in Fig. 4.20.)

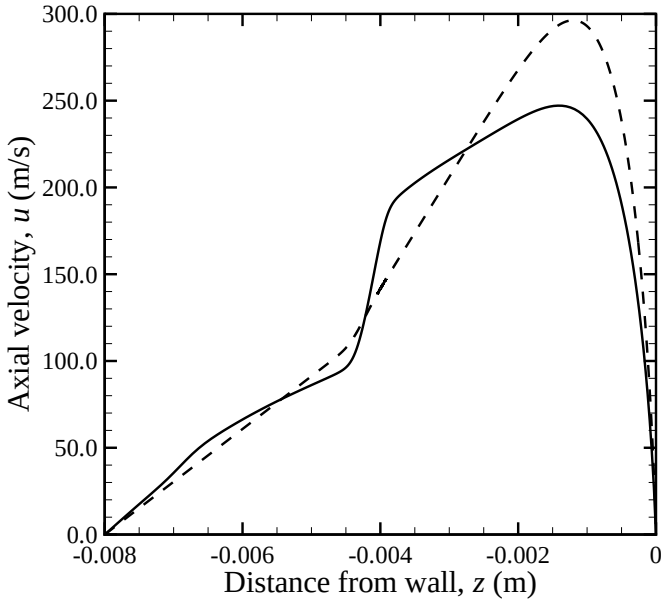

Figure 4.27: Comparison of the spreading rate (radial velocity gradient) profile between two-dimensional model (Case B120-10) and one-dimensional model (Case A120-10), using the same kinetics mechanism, for $\Phi = 1.20$.

4.2.2.2 Simulation of the stagnation flame in the laboratory and validation of the chemistry model

The discussions in this section focus on the capability and limitation of methane combustion models, such as GRI-Mech 3.0. As explained above, it is not a computational code that must be validated, but a model in the code that must be validated against experimental data to measure the modeling error. This is, to our knowledge, the first attempt to investigate the validity of a detailed methane chemical-kinetic model using multi-dimensional simulations with a realistic transport model that takes into account differential-diffusion effects.

The computational domain used for this study is shown in Fig. 4.28. It includes the interior and the exterior of the nozzle-plate assembly at the dimensions specified in the corresponding laboratory setup (Bergthorson, 2005; Benezech *et al.*, 2006). The combustible mixture is introduced at the bottom of the nozzle (the lower-left end) and a moderate amount of air is introduced at the bottom of the exterior between nozzle and the enclosure (the upper-left end) to accomodate the entrainment requirements of the jet flow. To stabilize the flame, in both experiments and simulations, a small amount of nitrogen is introduced from an outer nozzle, for which an exit velocity profile is specified in the simulation since the nozzle-wall proximity effect is not important in this region. All fluids entering the computational domain exit from the side of the stagnation plate, which can be seen at the upper-right end in the figure.

Figs. 4.29 through 4.33 show the contour plots of the mass fraction of CH radical, the pressure field, the axial velocity, the divergence constraint, and the heat-release rate for $\Phi = 0.70$ (Case 11), respectively. Compared to the earlier case (Phase II), in which the velocity boundary condition is specified at the nozzle exit, this one has a dip in the flame shape, which is a consequence of the nozzle-flame proximity effect that modifies the velocity profile at the nozzle exit. This flame shape has been observed in the laboratory and provides additional qualitative comparison between experiments and simulations.

This can be seen clearly in the plot of the pressure-eigenvalue (Fig. 4.34) and that of the spreading rate (Fig. 4.35). The pressure eigenvalue profile now has a peak that is positive at the flame front rather than a negative-valued spike. This positive pressure eigenvalue creates a plateau in the spreading rate profile at around the flame front when the negative spread from the negative curvature and the positive spread from the heat release balance.

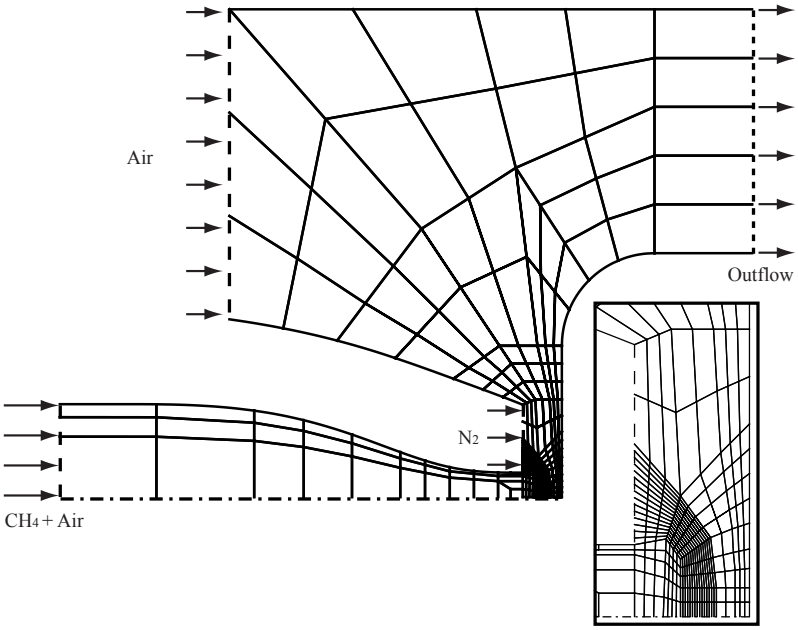

Figure 4.28: The computational domain and typical elements used for the simulation of stagnation flames of the laboratory experiments by Bergthorson & Dimotakis (2007). This computational domain contains 375 elements, and there are 12 by 12 collocation points within each element. Inflow/outflow boundaries can be recognized by the direction of the arrows. Note that the length of the arrows does not indicate the velocity magnitude. Solid lines on the boundary indicate solid isothermal walls, all of which are at $T_{\text{wall}} = 300$ K.

When the flame becomes stronger ($\Phi = 0.90$), the peak of the eigenvalue profile becomes large (Fig. 4.36) and the plateau of the spreading rate profile becomes a dip in the profile, as seen in Fig. 4.37.

As previously mentioned, the determination of laminar flame speeds is a major topic in laminar flame research. One of the main goals of this work is to conduct a numerical simulation that appropriately models the reacting flow observed in the laboratory so that a comparison of simulation and experiments can be done directly and appropriately. Shown in Fig. 4.38 is a comparison of the axial velocity profile obtained from the laboratory experiments by Bergthorson (2005) to the present simulation at an equivalence ratio of 0.70. The flow rate through the nozzle was not reported in the experiment, and was adjusted in the numerical simulation such that the nozzle exit velocity matches the first point in the measurements. The correction to the numerical data is applied to simulate the way in which the axial velocity field is measured in the laboratory, which is suggested in Bergthorson *et al.* (2005b) and Bergthorson (2005), and plotted as well to simulate PSV-measured

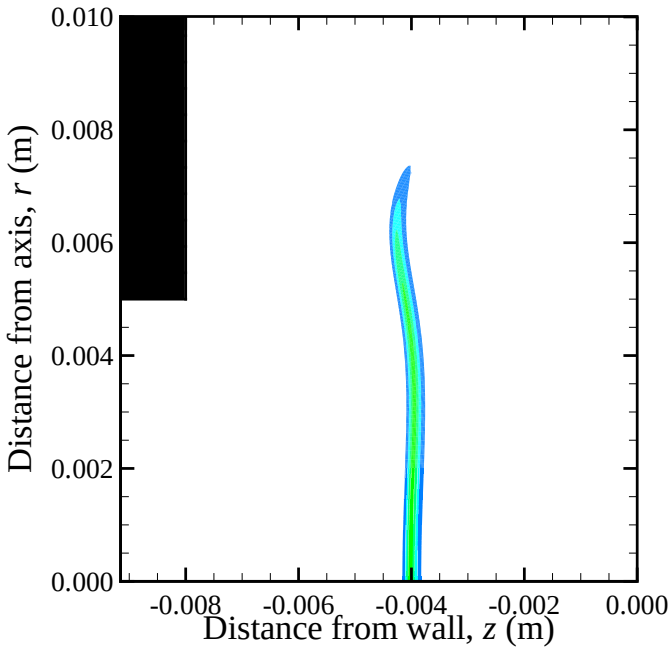

Figure 4.29: CH contour plot of lean flame ($\Phi = 0.70$). CH marks the chemiluminescence of lean flame and is used as a marker of the flame front in the laboratory. Note the flame has a dip in the middle due to nozzle-flame proximity effect. This can be seen in the laboratory.

velocity data from numerical simulation data. A *MATLAB*®script that simulates PSV is included in Appendix D of the present work. When the equivalence ratio is close to unity, a good agreement to experimental data is observed, as shown in Fig. 4.39. Qualitative agreement in flame shape can also be seen in Fig. 4.40, in which the experimental image of the flame shape through CH-PLIF imaging and computed CH contours are superimposed. Flame location and flame shape are both well-captured in the numerical result. For rich mixtures, GRI-Mech 3.0 with a two-dimensional model underpredicts inferred flame speed from that measured in a laboratory. Shown in Fig. 4.41 is a comparison of two-dimensional simulation to one-dimensional simulation. Due to lack of sufficient data in both experiments and simulations, there is no direct comparison for this case, however, from previous work (Bergthorson *et al.*, 2005b; Bergthorson, 2005), it is known that one-dimensional simulation tracks experimental data well. Provided that one-dimensional simulation with GRI-Mech 3.0 follows experimental mesurements, Fig. 4.41 implies GRI-Mech 3.0 underpredicts flame speed at this equivalence ratio of $\Phi = 1.20$.

Reference flame speeds are computed both from simulations and from measurements,

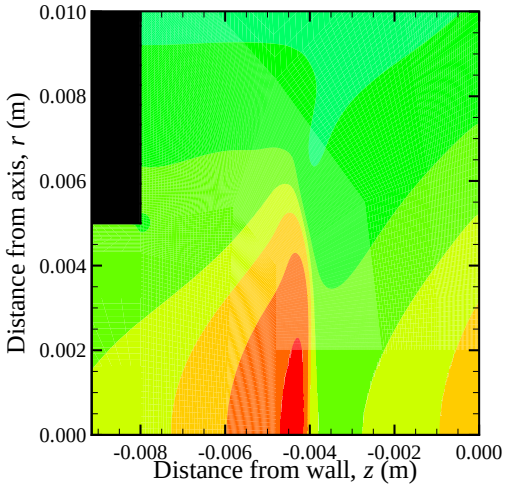

Figure 4.30: Pressure contour. Note that pressure has a large peak just upstream of the flame. The increased static pressure is fed into the nozzle, which causes the axial velocity deficit, and creates a negatively curved flame.

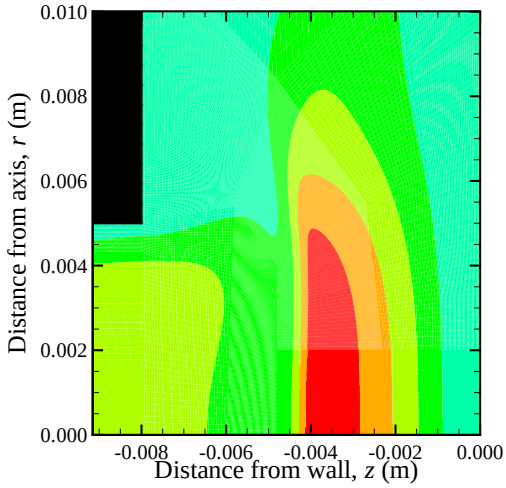

Figure 4.31: Axial velocity contours. Note curvature of iso-velocity lines in the vicinity of the flame.

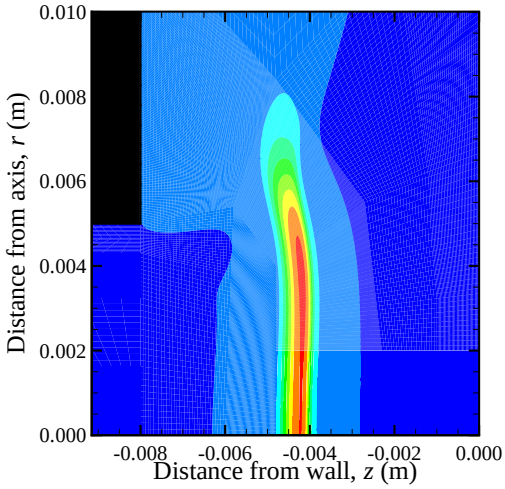

Figure 4.32: Contours of the divergence field

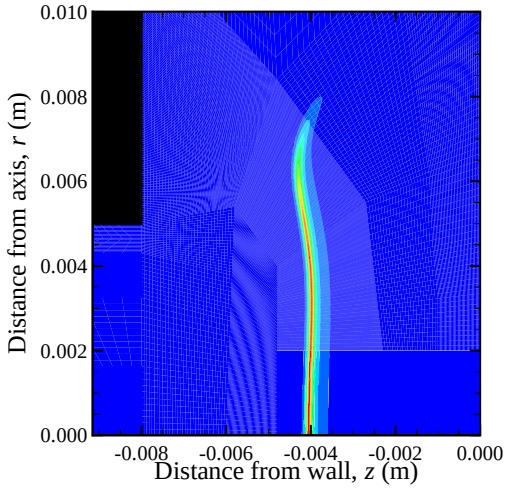

Figure 4.33: Contours of the heat-release rate

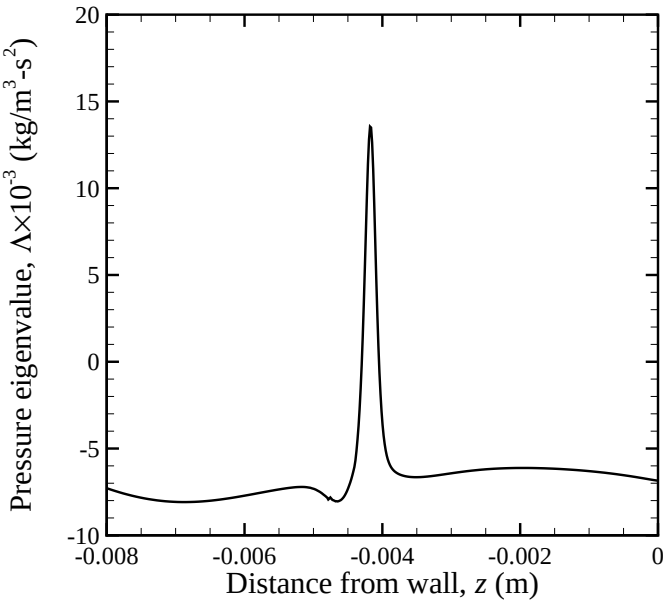

Figure 4.34: The pressure eigenvalue profile for $\Phi = 0.70$ (Case 11). The profile contains a sharp peak at the flame front.

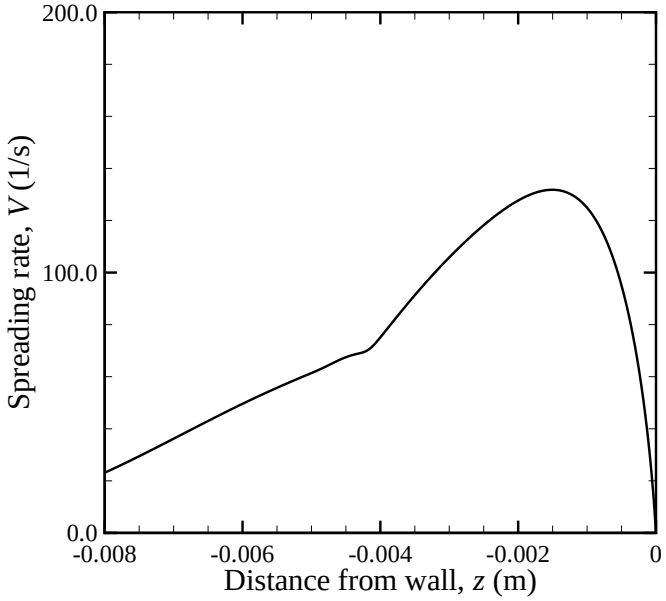

Figure 4.35: The spreading rate profile for $\Phi = 0.70$ (Case 11). A near plateau can be observed between $z = -0.0045$ and $z = -0.004$.

and compared to estimate modeling errors in the GRI-Mech 3.0 chemical kinetics model. Shown in Fig. 4.42 is the range of error at three different equivalence ratios when compared to experimental data reported in Bergthorson (2005). The model works well near the

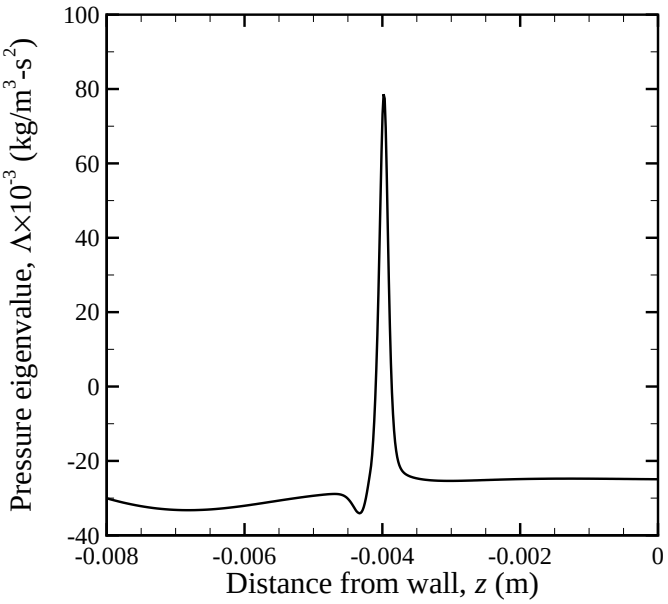

Figure 4.36: Pressure-eigenvalue profile for $\Phi = 0.90$ (Case 3). The peak of the profile is larger compared to that for a weaker flame (cf. Fig. 4.34).

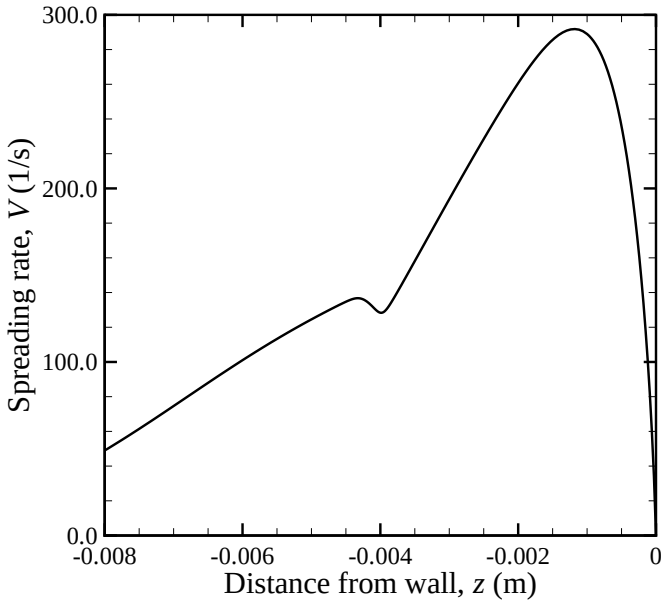

Figure 4.37: Spreading rate for $\Phi = 0.90$ (Case 3). The dip of the profile is the signature of negative flame curvature.

stoichiometric conditions while exhibiting as much as 10% error in lean and rich limits. This result is slightly different from a conclusion drawn in Bergthorson *et al.* (2005b) who relied on one-dimensional simulations. When experimental data are compared to the one-

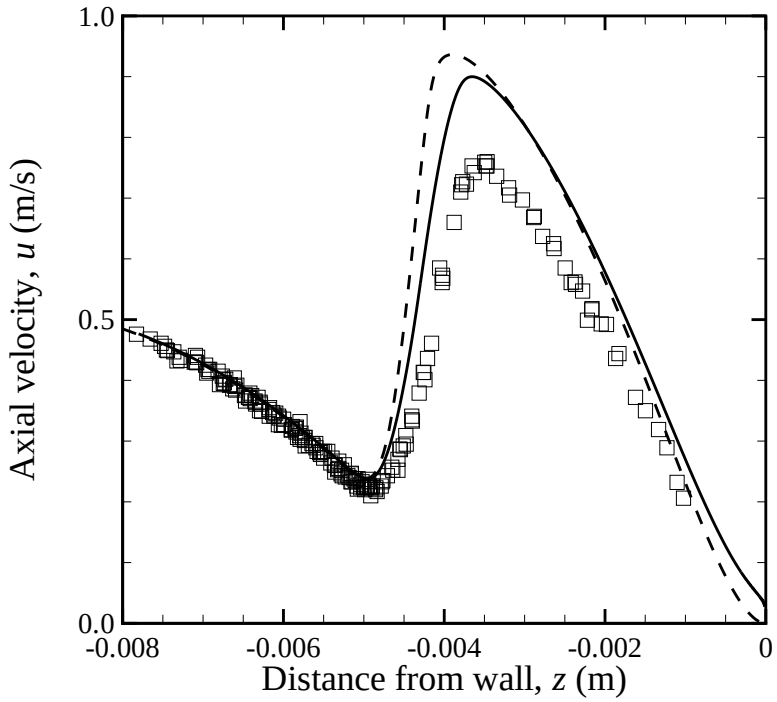

Figure 4.38: Axial velocity profile comparison between simulation and measurements for $\Phi = 0.70$. Squares denote experimental data (Run 212) from Bergthorson (2005), dashed lines are the results of a two-dimensional simulation (Case C070-11), while the solid line is a simulated PSV-measured velocity profile.

dimensional solutions, the results agree well except at lean conditions. On the other hand, intuitively, GRI-Mech may work better on the lean side because it contains a smaller subset of C-2 and C-3 compounds, and reactions involving them. The present work indicates GRI-Mech needs to be improved in a rich mixture case while it also indicates that the mechanism requires more work on the lean side; the latter is the same conclusion reached in Bergthorson *et al.* (2005b).

Turányi *et al.* (2002) found that the uncertainty in flame velocity is typically 2–5 cm/s, considering uncertainty in both thermodynamic and kinetic parameters, but caused mainly by rate constants. Considering less than 10% error at $\Phi = 0.70$ is at the lowest range in the uncertainty, this level of discrepancy between simulation and experiments is reasonable. To obtain further accuracy, as recommended by Turányi *et al.* (2002), rate constants for several important key reactions and thermodynamic data of certain radicals such as hydroxyl radicals need to be examined.

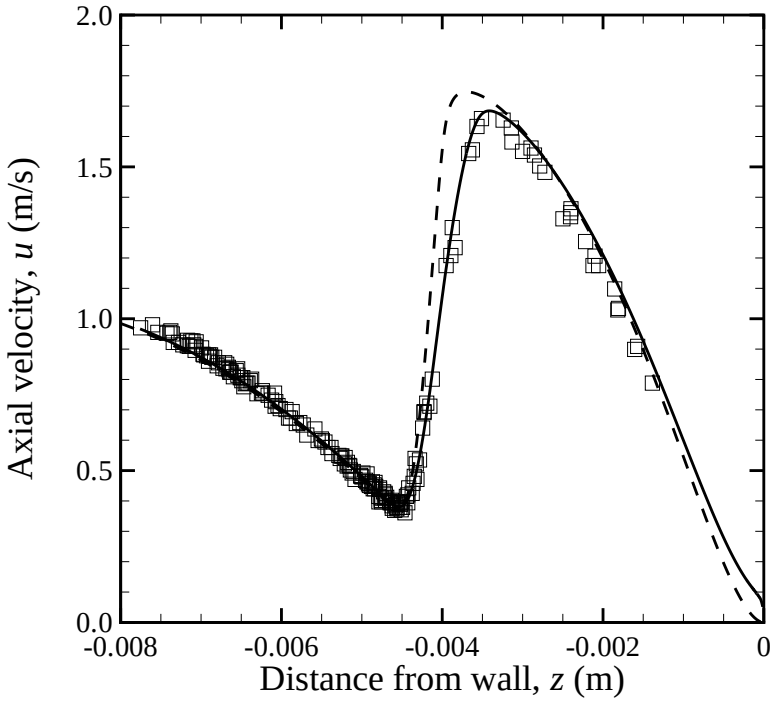

Figure 4.39: The axial velocity profile comparison between simulation (Case C090-4) and measurements (Run 206) from Bergthorson (2005) for $\Phi = 0.90$. (Legend as in Fig. 4.38

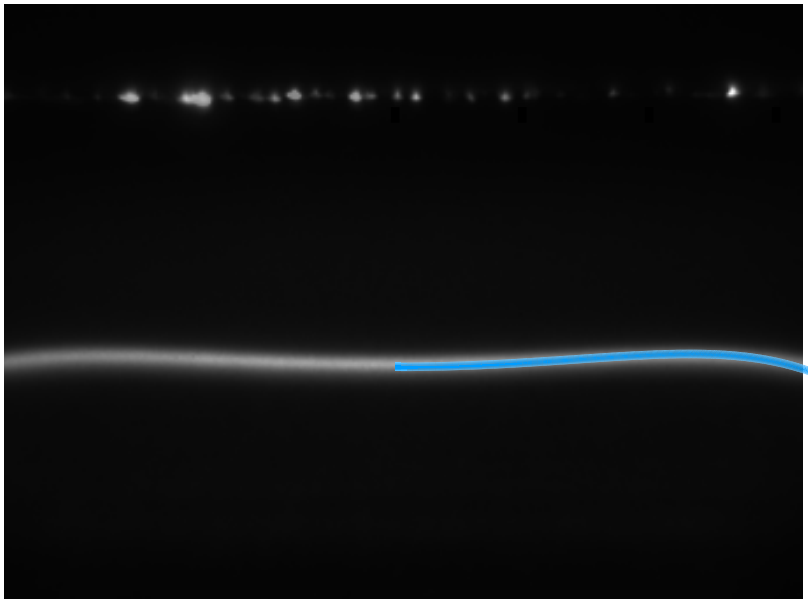

Figure 4.40: The experimental CH-PLIF image from Run 206 ($\Phi = 0.90$), reported in Bergthorson (2005), with computed CH contours (blue) superimposed on the right half. The experimental image is an average of 1,000 instantaneous exposures.

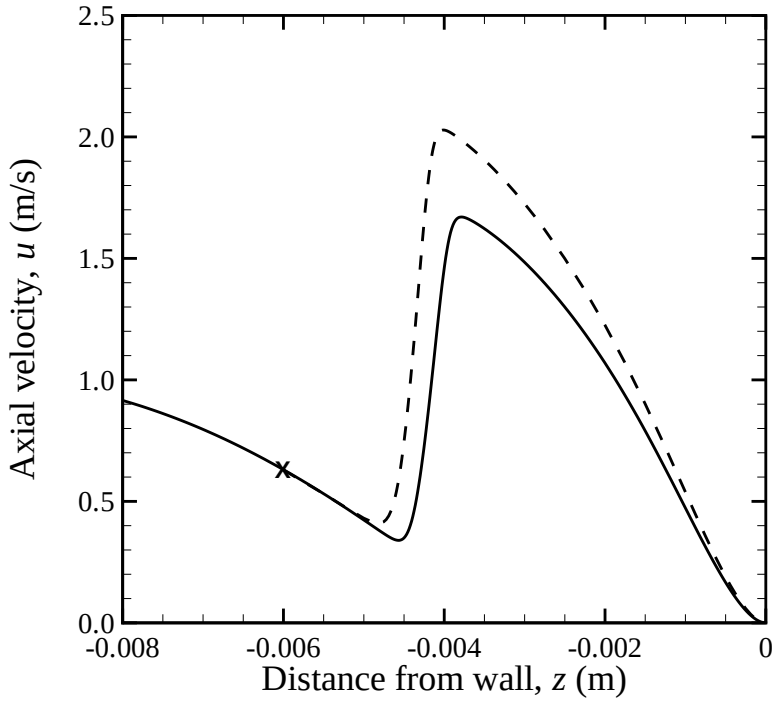

Figure 4.41: The axial velocity profile comparison between simulation (solid line, Case C120-1) and one-dimensional simulation (dashed line). The latter is known to track experimental data well for $\Phi = 1.20$ (Bergthorson, 2005).

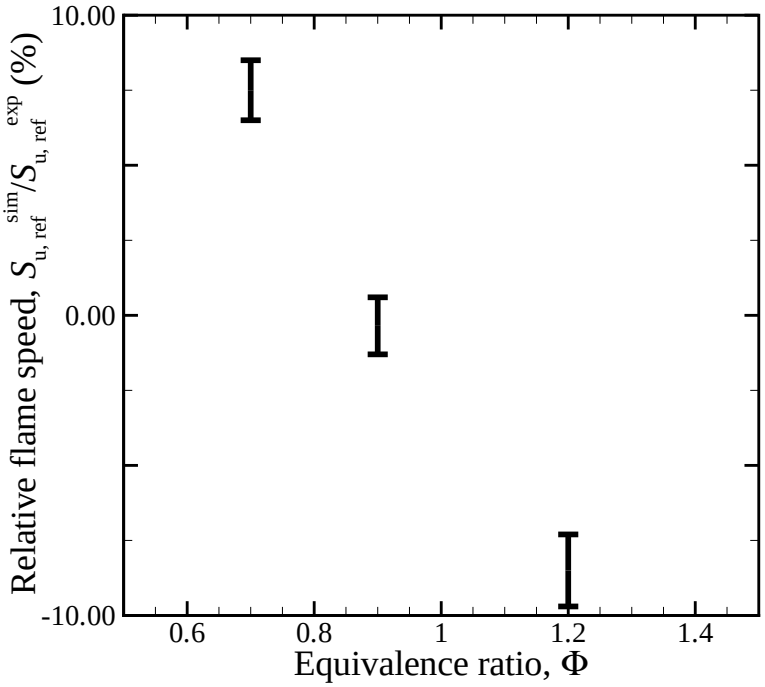

Figure 4.42: Variance between simulated reference flame speed and measured reference flame speed. The model works well near stoichiometric conditions, but there is a variance as high as 10% for rich and lean flames. This result is slightly different from a conclusion drawn in Bergthorson *et al.* (2005b) in which GRI-Mech agreed well with one-dimensional results. The agreement between experimental data and one-dimensional simulation data can be seen in Fig. 4.56 below.

4.2.2.3 Flame speed modification due to external conditions

In the last two sections, the validity of the one-dimensional model and the GRI-Mech 3.0 chemical kinetics model are assessed. The purpose of the current and following sections are to study the behavior of the flame itself numerically. The laminar flame speed, S_u^0, is an important parameter in laminar flame theory, yet a direct measurement of such a quantity is almost impossible. The laminar flame speed is defined as the terminal velocity of a one-dimensional planar, adiabatic flame, propagating into a quiescent unburnt, premixed, combustible mixture. In numerical computation, this quantity can be obtained as the solution to an eigenvalue problem for a premixed flame. However, due to the difficulty of making a direct measurement, many estimates rely on other measurements. The flame burning velocity varies because of various factors such as strain, stretch, curvature of the flame front, heat loss and so on. For the case of stagnation-stabilized flames, Egolfopoulos *et al.* (1997) studied the effect of the stagnation wall and found that it is unimportant as long as the flame is not close to the wall, so that the heat loss to the wall is insignificant. Those simulations relied on the EDL92 (Egolfopoulos *et al.*, 1992) and GRI-Mech 1.2 mechanisms. The discussion following confirms these findings, based on the GRI-Mech 3.0 model, which is used throughout the present study.

Fig. 4.43 shows the effect of the stagnation wall temperature at $\Phi = 0.70$. As can be seen: as the wall temperature rises, the rolling-off part of the curve straightens up, leading to an almost linear profile through a wide range of strain-rates. As pointed out by Egolfopoulos *et al.* (1997), at low enough strain-rates and with flames stabilized far enough from the wall, the impact of wall temperature on flame behavior is minor. However, the question remains: how far is far enough? Shown in Fig. 4.43 is reference flame speed against flame location. As can be seen, the flame propagates faster as wall temperature rises. Wall temperature does affect flame location. As wall temperature rises, the flame burning velocity increases, but at the same time, it projects itself on the characteristic strain-flame speed correlation by finding a right spot on that curve. Another thing to add to the earlier study is that even after the wall temperature is raised, the extrapolation of the strain-flame speed curve does not lead to the laminar flame speed, S_u^0, as can be seen in Fig. 4.43. An earlier study, Egolfopoulos *et al.* (1997) proposed:

> Therefore, it is proposed that the single jet-wall configuration can be used as an

alternative technique for the S_u^0 determination. However, the caution is required to assure that the flame is not affected by the wall as indicated by the "bending" of the $S_{u,ref}$ profile, and that data over a wide range of K[†] are obtained as close to $K = 0$ as possible in order to assume a more meaningful extrapolation.

However, it does not seem the laminar flame speed is on the linear extrapolation of reference velocities when $S_{u,ref}$ is plotted against strain-rate. When $S_{u,ref}$ is plotted against flame stretch instead of strain-rate, this conclusion makes sense, as shown in Fig. 4.45. In the ideal laminar flame speed calculation using a freely propagating flame model, both strain and stretch are zero due to the one-dimensional nature of the model. Shown in Figs. 4.46 through 4.49 are the reference flame speed, $S_{u,ref}$ from Cantera, plotted against the flame stretch, $\Gamma = \sigma_t(x_F)$. Note that these results do not include flame curvature. When the flame is curved, a modification is necessary, as discussed in the next section.

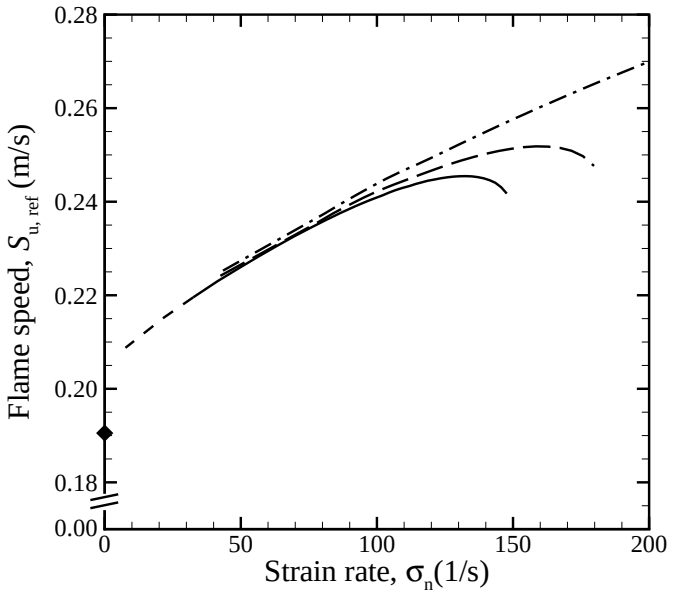

Figure 4.43: The effect of the stagnation wall temperature ($\Phi = 0.70$) studied by one-dimensional model with GRI-Mech 3.0 kinetic model at three different wall temperatures: $T_{wall} = 300\,K$ (solid line), $T_{wall} = 1000\,K$ (long dashed line), and $T_{wall} = 1700\,K$ (dot-dashed line). As T_{wall} approaches the adiabatic flame temperature, the relationship between strain and the flame speed is closer to linear. Short dash indicates cases where the flame is too close to the nozzle boundary condition and the flame data are affected by the nozzle temperature, which is set to 300 K.

[†] K in Egolfopoulos *et al.* (1997) denotes the strain-rate, σ, in this study

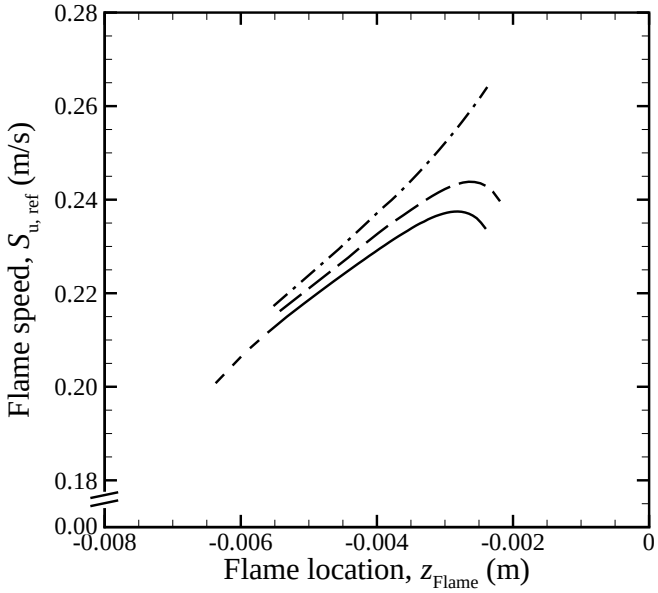

Figure 4.44: Although it does not appear on a σ - $S_{u,ref}$ plot, wall temperature influences where the flame stabilizes itself. When the flame is far enough from the wall, it does not affect the σ - $S_{u,ref}$ relationship. Therefore it is not possible to make a general statement as to what distance from the wall is far enough. (Legend as in Fig. 4.43)

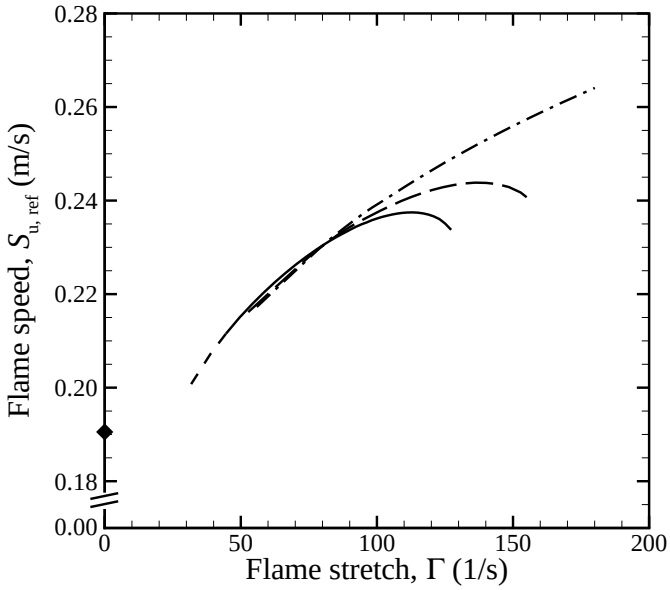

Figure 4.45: When the observed reference flame speed is plotted against flame stretch, it may be possible to estimate the laminar flame speed, S_u^0, by the extrapolation of the data to zero flame stretch at high wall temperature. (Legend as in Fig. 4.43)

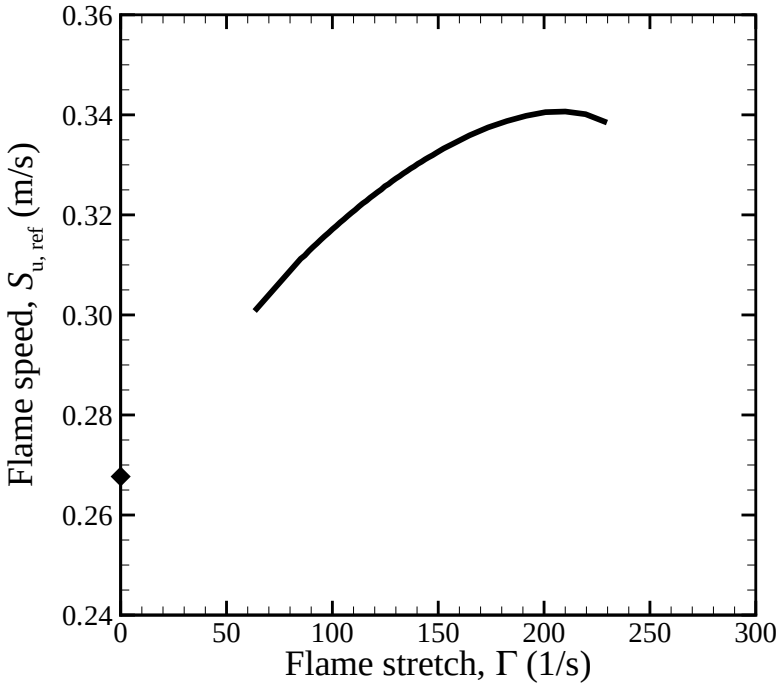

Figure 4.46: Reference flame velocity computed with the one-dimensional model for $\Phi = 0.80$ (solid line) and laminar flame speed, S_u^0 (♦)

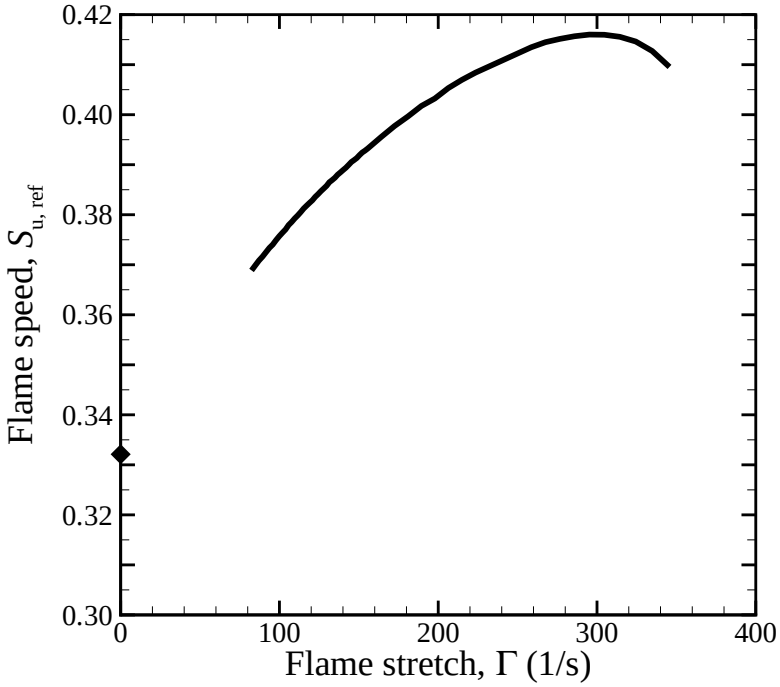

Figure 4.47: For $\Phi = 0.90$. (Legend as in Fig. 4.46)

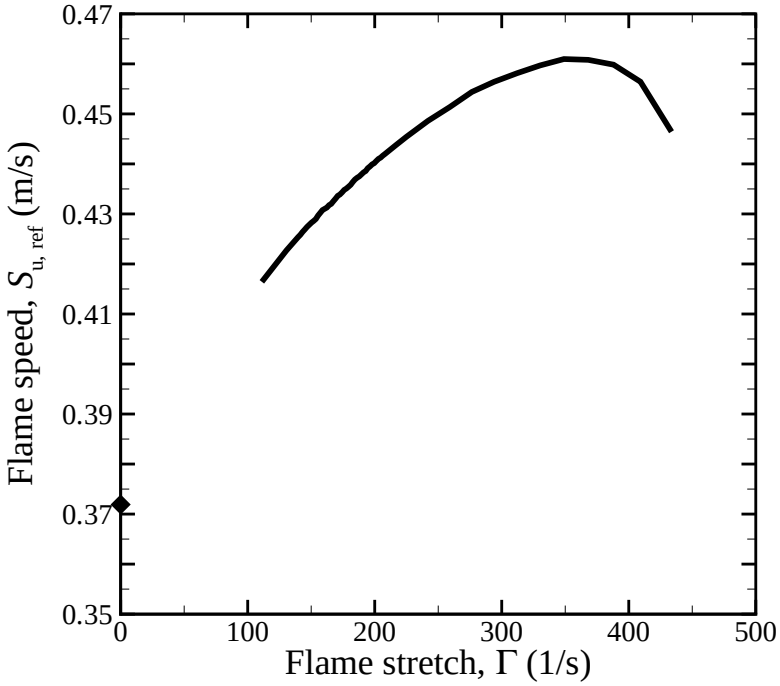

Figure 4.48: For $\Phi = 1.00$. (Legend as in Fig. 4.46)

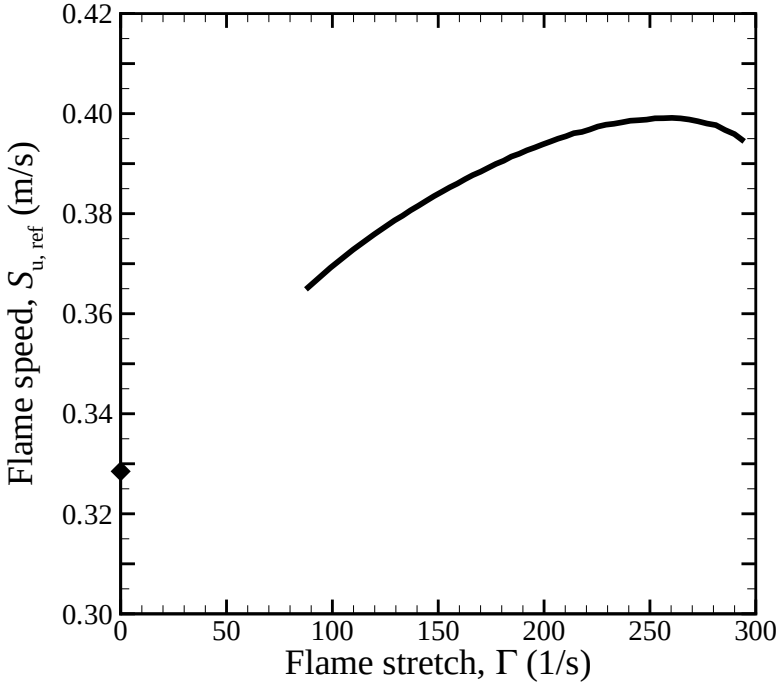

Figure 4.49: For $\Phi = 1.20$. (Legend as in Fig. 4.46)

4.2.2.4 Aerodynamic and geometric effects on flame speed

Interesting properties of a flamelet or a laminar flame are its propagation velocity and its variation with strain-rate (Law & Sung, 2000; Williams, 2000; Bergthorson, 2005), flame stretch (Wu & Law, 1984; Law, 1988; Vagelopoulos & Egolfopoulos, 1998), and curvature (Markstein, 1951; Matalon & Matkowsky, 1982). Flame propagation depends on various aerodynamic, thermodynamic, and chemical-kinetic conditions. However, these conditions are often interrelated, making it difficult to understand flame response to one condition alone. Both two-dimensional simulations and laboratory flames contain finite-curvature effects, whereas one-dimensional models do not.

Shown in Fig. 4.50 is a comparison of reference flame speed as a function of strain-rate for an equivalence ratio of 0.70. The reference flame speed is the local minimum velocity normal to the flame in the unburnt region, whereas the strain-rate is measured by the upstream absolute maximum velocity gradient, using standard definitions in the Community. The results from two-dimensional simulations and the one-dimensional model show the same trend: flame speed increases as strain-rates increase. The one-dimensional model predicts a somewhat concave shape, which is because of wall heat loss that is consistent with previous work by Egolfopoulos *et al.* (1997). The two-dimensional simulation data are clearly separated by the one-dimensional data. On one side, flames have a positive curvature (denoted as P), meaning they are concave towards the unburnt gas, while on the other side, flames have negative curvature (denoted as N). In this case, positive curvature leads to an increase in flame speed compared to a comparable one-dimensional case that has the same hydrodynamic strain. This modification of flame speed may be accounted for in terms of the phenomelogical model by Markstein (1951).

Landau (1944) and Darrieus, in analyzing the stability of plane flames, assumed that the behavior of wrinkled flames was not affected by the structure of the flame itself, leading to a flame that propagates at a uniform speed. This assumption led to their conclusion that plane flames are unconditionally unstable, which contradicts laboratory observations (see Matalon & Matkowsky, 1982; Clavin & Joulin, 1983). Markstein (1951) proposed that a local instantaneous burning velocity should depend on local instantaneous curvature of the

flame front only, which led to the phenomenological expression for the burning velocity,

$$\frac{S_n}{S_{\mathrm{u}}^0} = 1 + \mathcal{L}\kappa, \tag{4.8}$$

where S_n is the flame-normal propagation velocity, S_{u}^0 is the laminar flame speed at zero stretch and zero curvature, κ is the local curvature of the flame, and $\mathcal{L}$ is the Markstein length that is considered to be a characteristic length of the order of the flame thickness. Sometimes the Markstein length is scaled by the diffusion flame thickness to obtain the Markstein number, $Ma = \mathcal{L}/\delta_{\mathrm{flame}}$. In later work, Markstein (1964) recognized that it was the curvature of flame front relative to the curvature of the flow field that affects burning velocity and derived a more complete expression, which can be written as (following Clavin & Joulin (1983)):

$$\frac{S_{\mathrm{u,ref}}(\kappa)}{S_{\mathrm{u}}^0} = 1 + \mathcal{L}\left(\kappa + \mathbf{n}\cdot\nabla\mathbf{u}\cdot\mathbf{n}/S_{\mathrm{u}}^0\right), \tag{4.9}$$

where the first term is the effect of curvature, and the second term is the hydrodynamic stretch, which is related to the local stretch of the flame, Γ:

$$\Gamma \equiv \frac{1}{A}\frac{dA}{dt} = -\mathbf{nn} : \nabla\mathbf{u} + \nabla\cdot\mathbf{u} + S_L\nabla\cdot\mathbf{n}, \tag{4.10}$$

where $\mathbf{n}$ is the normal vector of the flame front pointing upstream, and S_L is the flame propagation velocity (which is zero in the case of stationary flames). Candel & Poinsot (1990) derived the above decomposition for flame stretch and noted that flame stretch has three contributions: the first term is because of the strain-rate, the second term is the volumetric expansion of the fluid, and the last term is because of the flame curvature. However, in the case of a stationary flame, the above expression becomes,

$$\Gamma = \nabla_t\cdot\mathbf{u}_t, \tag{4.11}$$

i.e., the spreading rate evaluated at the flame front. The operator, ∇_t, is the flame tangential component of the ∇ operator (Chung & Law, 1984). The effect of curvature is implicitly included in Γ through the change in tangential velocity, whereas it was explicit for the non-steady flame as in Eqn.(4.10).

Matalon & Matkowsky (1982) and Clavin & Joulin (1983) derived the above expression

for flame speed using high activation energy asymptotics, assuming small strain. They clarified that there are two contributions to total stretch: one from curvature and one from hydrodynamic strain (non-uniformity of the underlying flow). However, as noted by Tien & Matalon (1991), flame speed depends on where the reference point is taken to measure it: for example, the location of the minimum velocity upstream of the flame (Wu & Law, 1984; Egolfopoulos *et al.*, 1997; Bergthorson *et al.*, 2005b), that of the velocity maximum (Mendes-Lopes & Daneshyar, 1985), or the linearly or quadratically extrapolated velocity at the maximum heat release (Davis *et al.*, 2001; Deshaies & Cambray, 1990). Tien & Matalon (1991) investigated the implications of choosing three different reference points and found that when the downstream edge of the preheat zone is used as the reference location, flame speed indeed decreases with increased stretch, whereas when the velocity minimum is used, flame speed increases with increased stretch. In the present study, the location of minimum velocity upstream of the flame is used. The flame-speed measure at this location is different from the one used in the above analysis, and care must be taken to interpret the data consistently with this difference. Furthermore, previous work assumed only a small perturbation from a planar flame, and the correction term is on the order of $\epsilon = \delta_{\text{flame}}/L$, where δ_{flame} is the flame thickness and L is the length scale of the problem; these are typically on the order of $10^{-4}\,\text{m}$ and $10^{-2}\,\text{m}$ for the cases considered here, respectively.

Since the curvature effect can be accounted for by Markstein's model, Eqn. (4.8), we correct the curvature effect on flame speed through the following equation:

$$S_{\text{u,ref}}^{\kappa=0}(\sigma) = \frac{S_{\text{u,ref}}(\sigma,\kappa)}{1+\mathcal{L}\kappa} \tag{4.12}$$

to obtain flame speeds that should be observed in the absence of flame front curvature. This equation implies a slight modification to the originally proposed relation. The original equation as well as its extension by Matalon & Matkowsky (1982) and Clavin & Joulin (1983) assumed a planar freely propagating flame, and its perturbation from such an ideal state is described by the equations proposed by them. Since these models are for flows with small strain, the idea here is to take a curvature-free strain-stabilized flame as a reference state instead of planar freely propagating flame as was done in Markstein's original work. Curvature effects should still appear in the same manner at leading order. Bradley

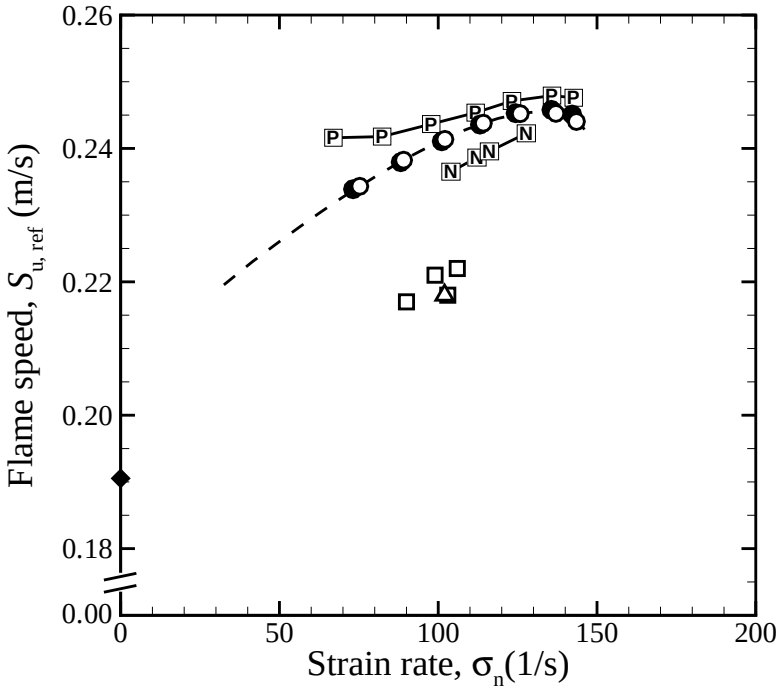

Figure 4.50: Comparison of calculated flame speed as a function of strain-rate, at an equivalence ratio of 0.70. (P): Two-dimensional simulations (Phase II, $\kappa > 0$); (N): Two-dimensional simulations (Phase III, $\kappa < 0$), (dashed line): One-dimensional simulations with plug-flow BC; (□): measurements by Bergthorson (2005); (△): measurements by Benezech *et al.* (2006), (⧫): Laminar flame speed computed using a one-dimensional freely propagating flame model. Circles indicate the cases corresponding to Phase II simulations, with the white ones indicating the plug-flow BC (1D) while the black ones indicate the slope-matched BC (1D-s).

et al. (1996) conducted a numerical simulation of one-dimensional spherically propagating methane flames using a reduced mechanism to estimate the Markstein number, Ma, for several different mixtures. They have found that Markstein numbers for curvature and stretch are different. Therefore, instead of a single number, Ma, there are Ma^c for curvature and Ma^s for stretch term. Using their Markstein number for curvature, Ma^c, of methane at $\Phi = 0.70$, 1.47, the right-hand side of the above equation can be calculated. This can remove the curvature effect from the observed reference flame speed, $S_{\mathrm{u,ref}}$. The result is plotted in Fig. 4.51. This correction method seems to work well and can organize differently curved flames into a single-variable description, permitting flame behavior to be discussed in terms of strain-rate only. It should be pointed out that it should be possible to apply the same method to experimental data. Curvature of the flame front can be estimated by

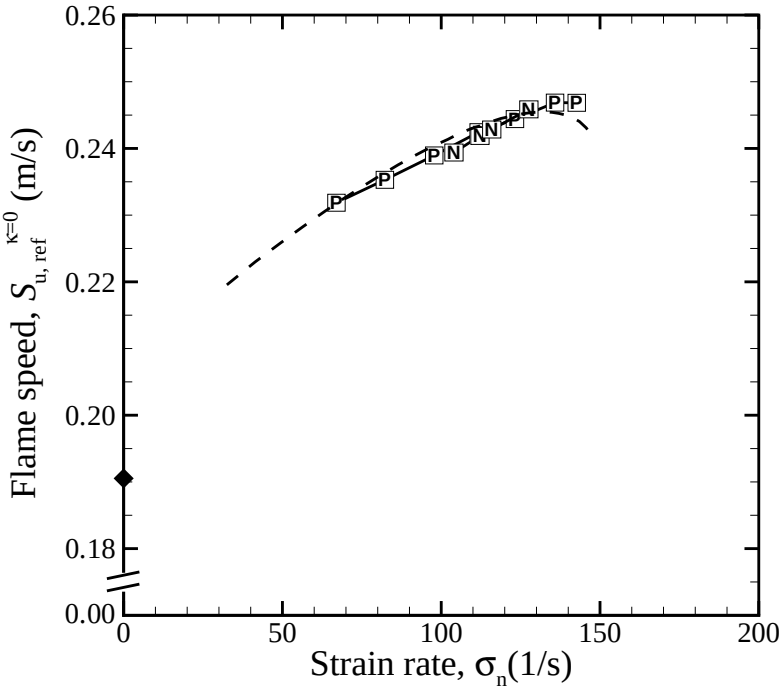

Figure 4.51: Curvature effect is corrected through Markstein's model using the previously reported Markstein number of 1.47 for $\Phi = 0.70$. Legends as in Fig. 4.50.

fitting a circle or polynomial to the CH-PLIF image, shown in Fig. 4.40, for example.

As noted earlier, it may be useful to study flame behavior in terms of flame stretch, instead of the strain-rate of the flow field. This is particularly true if a connection between flame speed obtained from strain-stabilized flame and freely-propagating flame is considered. However, when the flame is curved, attention must be paid to the appropriate stretch that is used to organize the data. To better understand the behavior of flames under stretch, we decompose stretch into two components, similar to the decomposition of flame stretch by Candel & Poinsot (1990), but for the steady case:

$$\Gamma = \Gamma_{1D} + \Gamma_c \tag{4.13}$$

where Γ_{1D} is a contribution from strain-rates (non-uniformity of the flow) and dilatation, while Γ_c is from curvature. Fig. 4.52 plots flame stretch vs. strain-rate for an equivalence ratio of 0.70. It can be seen that Γ_c is positive for positively curved flames and Γ_c is negative for negatively curved flame, provided $\Gamma_c = 0$ in the one-dimensional model. If curvature effects can be corrected through Markstein's model, $\Gamma_{1D} = \Gamma - \Gamma_c$ must be used to organize

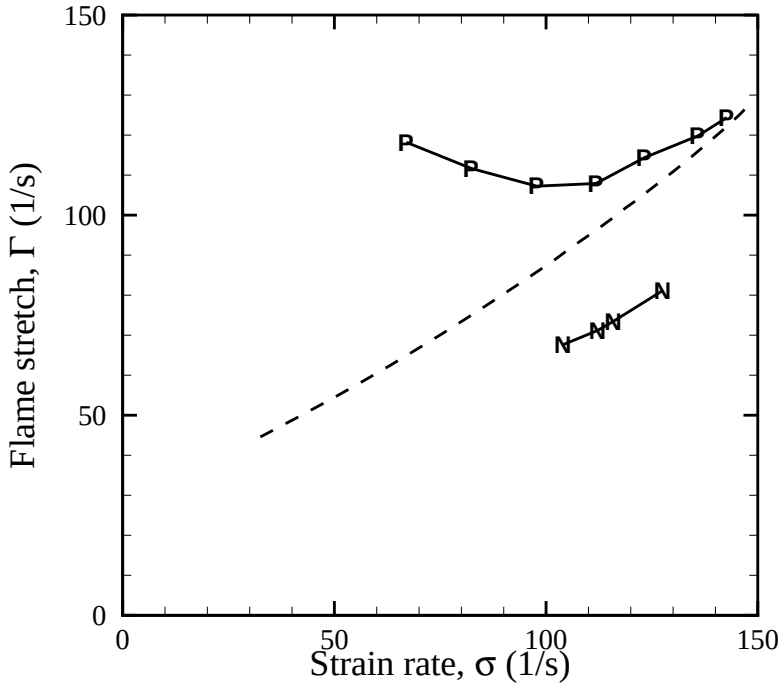

Figure 4.52: Flame stretch (Γ) as a function of the strain-rate (σ) for $\Phi = 0.70$. The two-dimensional simulation data with positive curvature (P) asymptote to the results from the one-dimensional model, as flow rate (and strain rate) increases. Since the one-dimensional model contains no curvature, the contribution of stretch below the curve of the one-dimensional model data is from dilatation, while the contribution above it is from the geometric curvature effect.

flame speed data, instead of the total stretch, Γ. Then, the following equation

$$S_{\mathrm{u,ref}}^{\kappa=0}(\Gamma_{\mathrm{1D}}) = \frac{S_{\mathrm{u,ref}}(\kappa,\Gamma)}{1+\mathcal{L}\kappa} \tag{4.14}$$

can be extrapolated so that $S_{\mathrm{u,ref}}^{\kappa=0}(0) = S_{\mathrm{u}}^{0}$. This is necessary because, although increasing curvature and increasing aerodynamic strain rate both lead to increased flame stretch and increased flame speed, they contribute at a different rate, unlike the asymptotic model that Eqn.(4.9) predicts.

However, as equivalence ratio increases, flame speed obtained from the one-dimensional simulations deviates from a region bounded by flame speeds of positively curved and negatively curved flames of the two-dimensional simulations, although positively curved flames still propagate faster than negatively curved flames. Shown in Figs. 4.53–4.56 are the results from $\Phi = 0.80$, 0.90, 1.00, and 1.20, respectively. Results for $\Phi = 0.90$ are scaled by an

appropriate Markstein number taken from Bradley *et al.* (1996), as was done for the case of $\Phi = 0.70$, and shown in Fig. 4.57. This departure of one-dimensional from two-dimensional ones results appears to be caused by the finite extension of the flame in the two-dimensional simulation, which supports diffusion of species in the radial direction, another effect that is absent in one-dimensional models. This effect may be quantified by additional simulations with larger flame radius to assess effects of the flame size in radial direction.

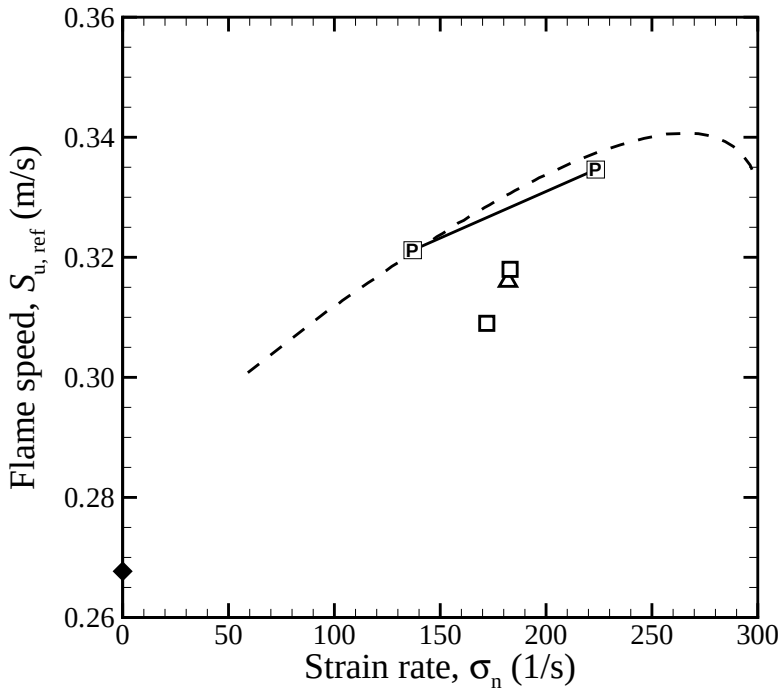

Figure 4.53: Comparison of calculated flame speed as a function of strain-rate, for an equivalence ratio of 0.80. (Legend as in Fig. 4.50.)

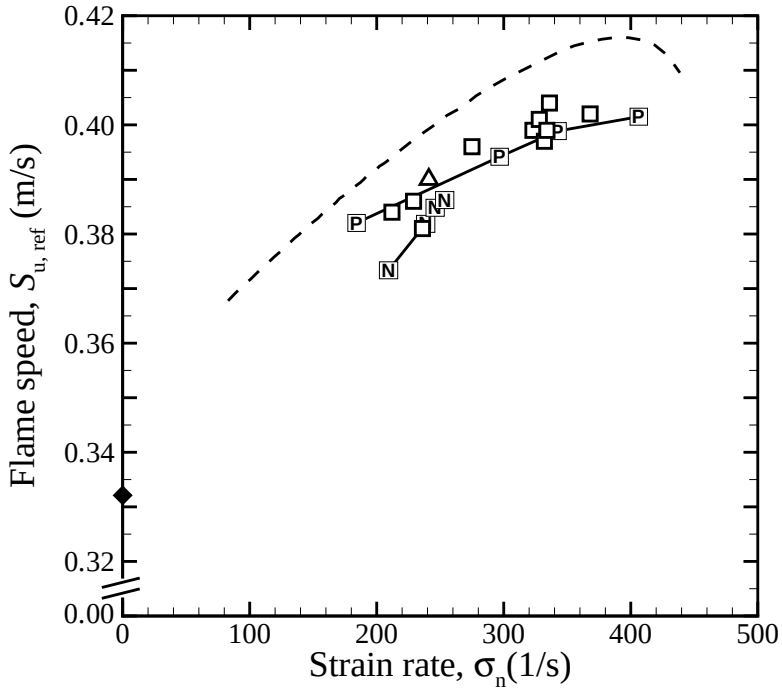

Figure 4.54: Comparison of calculated flame speed as a function of strain-rate, for an equivalence ratio of 0.90. (Legend as in Fig. 4.50.)

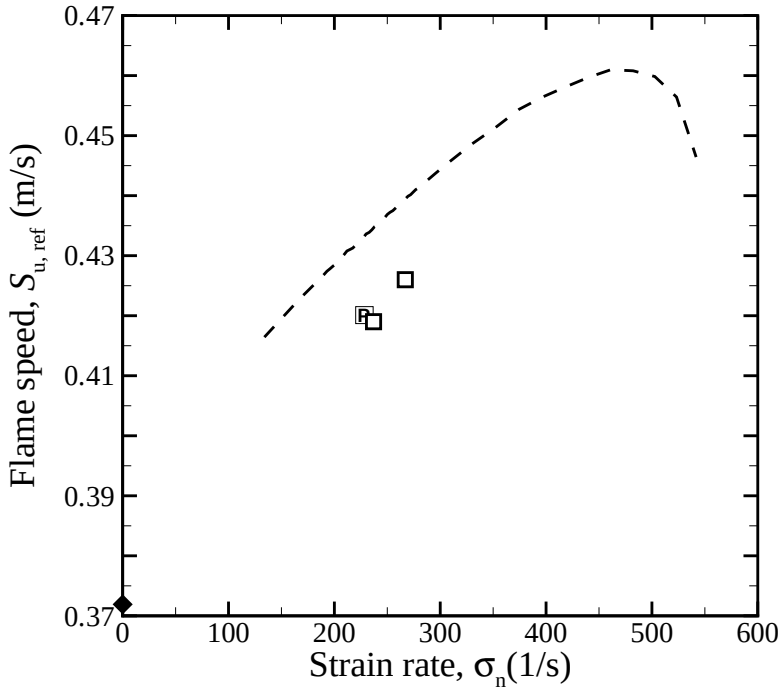

Figure 4.55: Comparison of calculated flame speed as a function of strain-rate, for an equivalence ratio of 1.00. (Legend as in Fig. 4.50.)

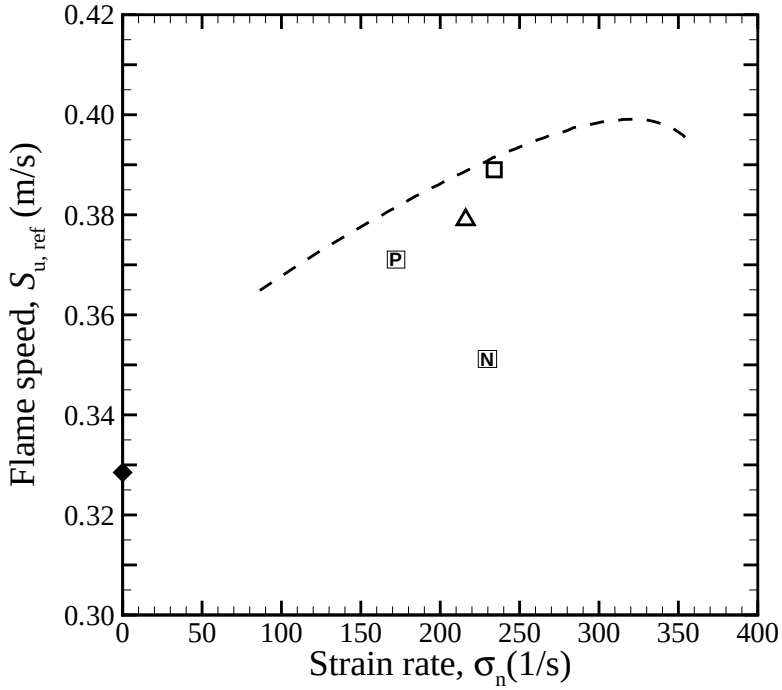

Figure 4.56: Comparison of calculated flame speed as a function of strain-rate, for an equivalence ratio of 1.20. (Legend as in Fig. 4.50.)

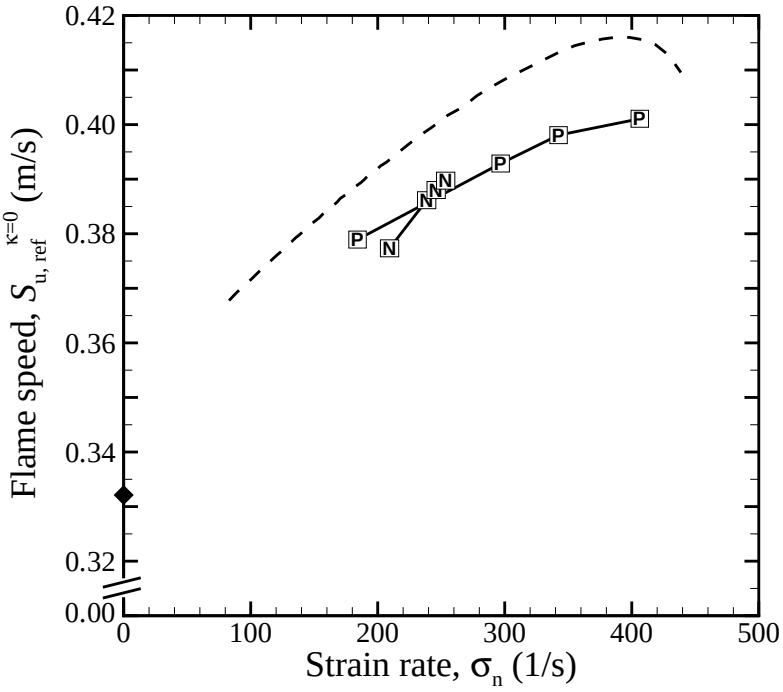

Figure 4.57: Curvature effect is corrected through Markstein's model with the previously reported Markstein number of 2.20 (Bradley *et al.*, 1996), for $\Phi = 0.90$. (Legends as in Fig. 4.50)

4.2.3 Summary

A comparison of experimental data and axisymmetric, two-dimensional simulations of the corresponding laboratory phenomena revealed that the methane combustion model based on GRI-Mech 3.0 works well for methane-air mixtures near stoichiometry. However, GRI-Mech 3.0 leads to an overprediction of laminar flame speed for lean mixtures, and an underprediction for rich mixtures. The latter is at variance with previous predictions based on one-dimensional models. This discrepancy stems from the fact that the one-dimensional model lacks the lateral diffusion of important species arising from the finite radius of curvature of the flames measured in the laboratory, and as simulated. The geometry of the flame front—such as the finite radius and finite curvature—is shown to have a significant contribution to flame propagation speed. In particular, Markstein's theory on the flame speed modification for flame curvature is confirmed by the present study as necessary for steady stagnation flames. At all equivalence ratios studied, Markstein length and Markstein numbers are always positive for methane-air mixtures, *i.e.*, positive curvature leads to faster flame propagation. There are some experimental (Deshaies & Cambray, 1990) and numerical (Davis *et al.*, 2002a,b) studies on the Markstein length, using stagnation flame or opposed-jet flames. In these reports, different definitions of flame speed and stretch are used from the ones used in the present study, and it more analysis is required to conclude whether the curvature effect that appears in the present study can be explained by the Markstein model and Markstein numbers previously reported. Currently, there is no consensus as to what the Markstein number is, and more experimental and numerical work, including two-dimensional simulation using full chemistry, appear necessary to settle such issues. Once settled, such information may be used to adjust experimentally measured flame speeds so that the target data for chemical kinetics can be organized without contamination by curvature effects.

A one-dimensional model with plug-flow boundary condition does not yield satisfactory results when a prediction of flame location is important. However, it is useful in providing a flame-speed to strain-rate relationship because the velocity boundary condition has an insignificant impact on flame location relative to local flow conditions. For this purpose, the plug-flow boundary conditions may be used. However, its comparison with experimental data requires some caution, because of effects not accommodated in the one-dimensional

model, such as the finite radial extension and the finite curvature of the flame.

Chapter 5

Conclusion

In the end, a theory is accepted not because it is confirmed by conventional empirical tests, but because researchers persuade one another that the theory is correct and relevant.—Fischer Black

5.1 Concluding remarks

A new algorithm for unsteady chemically reacting flow has been developed and implemented. The code has undergone verification tests to ensure the correctness of the obtained numerical results. In the process, a new basis function set for use in the axisymmetric spectral element method has been developed that incorporates the proper parity condition near the axis. This new basis function is an extension of early works by Leonard & Wray (1982) and Matsushima & Marcus (1995) for spectral methods. The resulting computing framework was used to study the behavior of non-reacting impinging jets and chemically reacting premixed methane flames in stagnation flow. The spectral element method was proved useful in the simulation of laboratory-scale flames, since it can accommodate the details of the experimental setup without sacrificing accuracy. Its extension to large density variations and reacting flow also proved successful.

For cold flow, a one-parameter model that describes the centerline velocity profile of the impinging jet is obtained, in collaboration with other researchers via synergetic efforts between experiments and computations (Bergthorson *et al.*, 2005a). This model can be used to specify an appropriate boundary condition for the one-dimensional model. In particular, the simulation played a key role in obtaining a new scaling law in terms of an effective nozzle diameter.

In the case of reacting flow, variances arising from the use of the GRI-Mech 3.0 chemical

kinetic model were quantified, and it was shown to work well near stoichiometric conditions. This comparison was made possible by accomodating every important factor in the experimental setup and is the first direct comparison of laboratory measurements and numerical simulations on the stagnation flames. The result of the comparison shows that the GRI-Mech 3.0 chemical kinetics model could be improved, at least for lean and rich methane mixtures. The conclusion for rich mixtures is new and differs from previous estimates that were obtained by comparing experiments and one-dimensional numerical solutions. This discrepancy is most probably caused by the fact that the one-dimensional model lacks the radial diffusion of important species due to its assumption of a flat (zero-curvature) flame of infinite extent. This effect does not seem to have been explicitly noted in previous studies that relied on one-dimensional hydrodynamics models to study stagnation flames, and more study is necessary to confirm and quantify the effect.

Flame-front curvature was shown to have a discernible effect on the resulting flame speed, and correction is necessary to have an accurate estimate of errors in chemical kinetics models in the future, or to obtain target flame-speed data from experiments used for kinetic rate parameter optimization. Although not recommended, if the extrapolation method is used to estimate laminar flame speed, this curvature correction is important as flames can have different curvatures for each single realization. Of course it would be more accurate to make comparisons and set benchmarking target for mechanism optimizations without flame speed extrapolations, as implemented by Bergthorson *et al.* (2005b). The fact that the estimation of Markstein numbers remains an on-going research problem may cause difficulty in adjusting flame speed to take curvature effects into account.

Using an axisymmetric two-dimensional simulation environment, it was shown that one-dimensional models can provide a flame-speed to strain-rate relationship because the velocity boundary condition has an insignificant impact on the flame speed itself although the prediction of flame location *is* sensitive to a choice of velocity boundary conditions.

Many results reported here have benefitted from the concurrent experimental and numerical work, conducted by a team, and such an approach was proven to be powerful and beneficial in understanding flame behavior, although it was not particularly easy to ensure that both the experimental and numerical details were in sufficient agreement to permit the quantitative comparisons performed.

5.2 Recommended future work

As noted in the first chapter, each methane combustion model includes a hydrogen reaction submechanism. Although much simpler, numerical results for hydrogen flames do not agree with each other (see Appendix E), implying slightly different behavior for each hydrogen submechanism of the hydrocarbon reaction mechanisms. However, one of the most important reactions in determining laminar flame speed of methane is (Williams, 2000),

$$H + O_2 + M \Leftrightarrow HO_2 + M.$$

Turányi *et al.* (2002) also pointed out seven elementary reactions that contribute to uncertainty in methane flame speeds. Two of them are in the hydrogen kinetic submodels: one is the above reaction, and the other is

$$O_2 + H \Leftrightarrow OH + O.$$

It would be useful to quantify errors in the hydrogen reaction subset of each model first, since the hydrogen submechanism is an important ingredient in hydrocarbon mechanisms, before attempting to optimize hydrocarbon kinetic models. Two-dimensional simulation of hydrogen flames are significantly less computationally expensive, and the Omega code can contribute to such developments. In particualr, extinction and reignition behavior of hydrogen flames is expected to be useful in assessing the behavior of chemical kinetics models. The experimental study by Pellet *et al.* (1998) may provide a useful target.

Although in two-dimensional simulations the entire flow field is obtained, the analysis of flame behavior is only discussed along the axis, where the detailed experimental data cited above were obtained. It would be interesting to extend the analysis in the off-axis regions along each streamline. This involves computation of curvature and flame stretch at off-axis locations. It is recommended to start this work for $\Phi = 0.90$ or stoichiometric conditions where experimental and numerical data agree, at least along the axis.

In terms of computing capability, one extension of the code would be to incorporate the multicomponent diffusion model (Curtiss & Bird, 1999; Hirschfelder *et al.*, 1954), including Soret effects in the species diffusion velocity, instead of using the simpler Fickian diffusion model. In particular, Ern & Giovangigli (1998) showed that Soret effects have an impact

on the structure of rich Bunsen flame. EGLIB developed by Ern and Giovangigli, which implements multicomponent transport algorithms, may be useful for this purpose (see Ern & Giovangigli, 1994).

Another useful approach would be to implement a Newton-Krylov method (see Gropp *et al.*, 2000) for solving nonlinear equations numerically. The current time-stepping approach will also be useful within the solution search algorithm as used in CHEMKIN and Cantera. In Chapter 2, it was shown that matrix reuse can save computational time significantly. A similar approach might work for Jacobians of chemistry ODEs. This approach has not been explored and may be worth investigating. Currently, the code makes no attempt in load balancing, and therefore, some processors are taking more elements that are heavily involved with chemical reactions while others are waiting to proceed. The load balancing in terms of the workload in chemistry ODE integration may lead to significant speedup of execution. Finally, the inclusion of a nonconforming mesh and an adaptive mesh refinement algorithm will make the code friendlier to those who do not have a lot of experience with numerical analysis, since allocation and distribution of elements are probably the most difficult task in using the current version of the Omega code, compared to the widely used Cantera program.